

A HIGHLY COMPLETE SPECTROSCOPIC SURVEY OF THE GOODS-N FIELD^{1,2,3}

A. J. BARGER,^{4,5,6} L. L. COWIE,⁶ W.-H. WANG^{7,8}

Published in The Astrophysical Journal (2008, 689, 687)

ABSTRACT

We present a table of redshifts for 2907 galaxies and stars in the 145 arcmin² *HST* ACS GOODS-North, making this the most spectroscopically complete redshift sample obtained to date in a field of this size. We also include the redshifts, where available, in a table containing just under 7000 galaxies from the ACS area with $K_{s,AB} < 24.5$ measured from a deep K_s image obtained with WIRCam on the CFHT, as well as in a table containing 1016 sources with $NUV_{AB} < 25$ and 478 sources with $FUV_{AB} < 25.5$ (there is considerable overlap) measured from the deep GALEX images in the ACS area. Finally, we include the redshifts, where available, in a table containing the 1199 $24\ \mu\text{m}$ sources to $80\ \mu\text{Jy}$ measured from the wider-area *Spitzer* GOODS-North. The redshift identifications are greater than 90% complete to magnitudes of $F435W_{AB} = 24.5$, $F850LP_{AB} = 23.3$, and $K_{s,AB} = 21.5$ and to $24\ \mu\text{m}$ fluxes of $250\ \mu\text{Jy}$. An extensive analysis of these data will appear in a parallel paper, but here we determine how efficient color-selection techniques are at identifying high-redshift galaxies and Active Galactic Nuclei. We also examine the feasibility of doing tomography of the intergalactic medium with a 30 m telescope.

Subject headings: cosmology: observations — galaxies: active — galaxies: distances and redshifts — galaxies: evolution — galaxies: formation

1. INTRODUCTION

Substantial progress has been made in tracing the formation and evolution of galaxies through extensive multiwavelength observations of extragalactic survey fields. However, the most challenging and time-consuming task is spectroscopically identifying the sources. This is especially true when one is trying to identify complete samples to faint magnitude limits. Although with existing multiwavelength data sets we can construct spectral energy distributions (SEDs) and measure photometric redshifts for galaxies, spectra provide an enormous amount of additional information on the sources. We have therefore carried out a very high quality, nearly spectroscopically complete, magnitude limited redshift survey of the Great Observatories Origins Deep Survey-North (GOODS-N; Giavalisco et al. 2004) field. The GOODS-N is one of the most intensively studied regions in the sky, and in many bandpasses it has the deepest images ever obtained. It has also been the target of extensive spectroscopic observations over the years (e.g., Cohen et al. 2000; Wirth et al. 2004; Cowie et al. 2004). Thus, it is nearly ideal for the present study.

In a parallel paper (Cowie & Barger 2008) we use this unique spectral database to place galaxies into the overall evolutionary scheme by combining spectral line and break

diagnostics with colors and by analyzing metal evolution. Here we present the data catalogs and use the redshift information to test the efficiency of using color-selection techniques to identify populations of high-redshift galaxies and Active Galactic Nuclei (AGNs). We also determine which AGNs can be distinguished by their colors. We then use the data set to examine the feasibility of doing intergalactic medium (IGM) tomography on a 30 m telescope.

Techniques have been developed to pre-select high-redshift candidates for spectroscopic confirmation using simple photometric selection criteria. The Lyman Break Galaxy (LBG) dropout technique (e.g., Cowie et al. 1988; Songaila et al. 2000; Lilly et al. 2001; Steidel & Hamilton 1993; Steidel et al. 1995) is the most heavily used of these and has really opened up the field to the study of $z > 3$ star-forming galaxies. However, with the advent of wide-area near-infrared (NIR) arrays, other selections, including the Distant Red Galaxy (DRG) color selection (Franx et al. 2003; van Dokkum et al. 2003; $z \gtrsim 2$) and the *BzK* color selection (Daddi et al. 2004; $1.4 \lesssim z \lesssim 2.5$), have recently become popular. The above selections are, of course, limited to sources that can be observed in optical and NIR surveys, but they have produced a substantial sample of spectroscopically confirmed high-redshift galaxies and AGNs. H^- methods using the mid-infrared (MIR) spectral shapes have also been suggested (e.g., Simpson

¹Based in part on data obtained at the W. M. Keck Observatory, which is operated as a scientific partnership among the the California Institute of Technology, the University of California, and NASA and was made possible by the generous financial support of the W. M. Keck Foundation.

²Based in part on data obtained at the Canada-France-Hawaii Telescope, which is operated by the National Research Council of Canada, the Institut des Sciences de l'Univers of the Centre National de la Recherche Scientifique, and the University of Hawaii.

³Based in part on data collected at the Subaru Telescope, which is operated by the National Astronomical Observatory of Japan.

⁴Department of Astronomy, University of Wisconsin-Madison, 475 North Charter Street, Madison, WI 53706.

⁵Department of Physics and Astronomy, University of Hawaii, 2505 Correa Road, Honolulu, HI 96822.

⁶Institute for Astronomy, University of Hawaii, 2680 Woodlawn Drive, Honolulu, HI 96822.

⁷Jansky Fellow.

⁸National Radio Astronomy Observatory (NRAO), 1003 Lopezville Road, Socorro, NM 87801. The NRAO is a facility of the National Science Foundation operated under cooperative agreement by Associated Universities, Inc.

& Eisenhardt 1999; Sawicki 2002). Although these techniques have not been heavily used, they are of considerable interest for optically faint sources.

With all of these avenues for finding high-redshift sources, we would hope that there are not still significant populations that remain unidentified. Recently, however, Le Fèvre et al. (2005) and Paltani et al. (2007) have challenged this view using the VIMOS Very Large Telescope Deep Survey (VVDS), a purely I flux-selected sample (targets have magnitudes between $I_{AB} = 17.5$ and $I_{AB} = 24$) of 9295 galaxies (“first epoch”) with measured redshifts in the range $0 \leq z \leq 5$. These authors claim surface densities consistently larger than those of Steidel et al. (1996, 1999, 2004) by factors of 1.6 – 6.2 at $z \approx 3$, with the largest factor applying to the brightest magnitudes. In calculating the surface densities they corrected for the fraction of galaxies they did not observe ($\sim 76\%$) and for their estimate of the fraction of galaxies with incorrect redshifts. The need for the latter correction arises from their use of redshifts with all four of their reliability flags (flags 3 and 4 have very reliable measurements; flag 2 has a reasonably reliable measurement, but there is a non-negligible probability that the redshift is wrong; flag 1 has a tentative measurement, but there is a significant probability that the redshift is wrong). They concluded that the LBG selection techniques and photometric redshift studies are not able to identify the full population of high-redshift galaxies found through spectroscopic observations of pure magnitude selected samples. This claim requires verification from a highly spectroscopically complete sample with very reliable redshift identifications.

A 30 m telescope will revolutionize wide-field spectroscopy, making sources that are currently 10 times too faint for moderate-to-high dispersion spectroscopy in the optical accessible and mapping the distribution of galaxies over the redshift range $2 \leq z \leq 4$. Of most interest, however, is whether a 30 m telescope will allow dense sampling of the IGM through the use of background galaxies. This would be an enormous improvement over the one-dimensional information now obtained through the study of rare high-redshift quasars, whose surface density on the sky at magnitudes accessible with Keck is very low. To trace the three-dimensional distribution of diffuse gas at high redshifts would require a high density of background probes, but it needs to be determined whether the necessary surface density of such probes exists.

The structure of the paper is as follows. In §2 and §3 we describe, respectively, our photometry and our spectroscopy. In §4 we examine how well different color selection techniques do, including LBG selection in §4.1, BzK selection in §4.2, and H^- selection in §4.3. In §5 we consider whether IGM tomography is feasible with a 30 m telescope, and in §6 we summarize our results.

We assume $\Omega_M = 0.3$, $\Omega_\Lambda = 0.7$, and $H_0 = 70 \text{ km s}^{-1} \text{ Mpc}^{-1}$ throughout. All magnitudes are given in the AB magnitude system, where an AB magnitude is defined by $m_{AB} = -2.5 \log f_\nu - 48.60$. Here f_ν is the flux of the source in units of $\text{erg cm}^{-2} \text{ s}^{-1} \text{ Hz}^{-1}$.

2. THE PHOTOMETRIC DATA

2.1. Optical Imaging

We take the optical photometric data from existing work. In particular, we take the U magnitudes from Capak et al. (2004) and the F435W, F606W, F775W, and F850LP magnitudes from the *HST* Advanced Camera for Surveys (ACS) observations of the GOODS-N (Giavalisco et al. 2004). There is an absolute offset in declination of $0''.4$ from the 20 cm VLA image of Richards (2000) to the ACS and *Spitzer* images, so we applied a $-0''.4$ offset to the ACS and *Spitzer* catalogs to make them consistent with the ground-based optical and NIR data and the X-ray and radio data, all of which are already in the VLA astrometric frame. All coordinates in the tables are given in the VLA astrometric frame.

2.2. Near-Infrared Imaging

We have obtained new ultra-deep K_s images from the Wide-field Infrared Camera (WIRCam) on the CFHT 3.6 m telescope and from the Multi-Object Infrared Camera and Spectrograph (MOIRCS) on the Subaru 8.2 m telescope. WIRCam covers the entire ACS and *Spitzer* GOODS-N regions in one pointing. The WIRCam image is an ~ 40 hr exposure and reaches a 5σ limit of $K_{s,AB} = 24.8$. MOIRCS has a smaller field of view, but we obtained an ultra-deep mosaic which covers nearly the full ACS area after including all available data in the Subaru archive. The MOIRCS image has a very non-uniform sensitivity distribution, but the image quality is extremely good ($0''.4 - 0''.5$ throughout). Although we cross-compared the WIRCam image with the MOIRCS image to eliminate artifacts and fragments of larger galaxies in constructing the catalogs, we measured the K_s -band magnitudes from the WIRCam image alone. Below we describe the WIRCam and MOIRCS observations and data reduction.

2.2.1. WIRCam Imaging

WIRCam consists of four $2k \times 2k$ HAWAII2-RG detectors covering a field of view of $20' \times 20'$ with a $0''.3$ pixel scale. K_s -band imaging observations were carried out by our group in the semesters of 2006A and 2007A and by a Canadian group led by Luc Simard in 2006A. The images were dithered to cover the detector gap and to obtain a uniform sensitivity distribution. Most of the observations were performed under photometric conditions with seeing between $0.6''$ and $1''$, and the total integration time was 39.7 hr.

The data were reduced in the Interactive Data Language (IDL) using the SIMPLE Imaging and Mosaicking Pipeline (SIMPLE, W.-H. Wang 2008, in preparation⁹). Images within a dither set (typically 15 min in length) were flattened using an iterative median sky flat in which a simple median sky was first derived to flatten the images and then a second median sky was derived by masking all of the detected objects using the flattened images. After the images were flattened, the residual sky background was subtracted from each image with a smooth polynomial surface fitted to the masked image. Crosstalk effects between each of the 32 readout channels on a detector were removed by subtracting the median of the 32 $64 \times 2k$ channels in the object-masked image. This removes most of the crosstalk and only weak residual features persist around the few brightest stars in the field. The small areas contaminated by the residual crosstalk are mostly outside the

⁹see also <http://www.aoc.nrao.edu/~whwang/idl/SIMPLE/index.htm>

ACS and *Spitzer* GOODS-N regions and are excluded in this work. The brightest cosmic ray hits were removed by a 5 pixel \times 5 pixel sigma filtering in each flattened image.

We used the SExtractor package (Bertin & Arnouts 1996) to measure the object positions and fluxes in each flattened, sky subtracted, and crosstalk removed image in a dither set. The first-order derivative of the optical distortion function was derived by measuring the offsets of each object in the dither sequence as a function of location in the images. Absolute astrometry was obtained by matching the detected objects to a reference catalog constructed with brighter and compact objects in the ACS catalog (Gavalisco et al. 2004; after correcting for the 0''.4 offset between the ACS and radio frames) and the SuprimeCam catalog (Capak et al. 2004). The reduced exposures were then warped directly from the raw frames to a common tangential sky plane with a sub-pixel accuracy. This projection corrects for both optical distortion and absolute astrometry. All projected images were weighted by their sky transparencies and exposure times and were combined to form a large mosaic. When images from a dither set were combined, a sigma filter was applied to pixels that have the same sky position to further remove fainter cosmic rays and artifacts such as reflections inside the optics. In the image combination the SExtractor fluxes of objects in the images were used to correct for variable extinction. Determining the absolute photometry of the WIRCam image is not straightforward because there were no standard star observations. Our initial attempt was to calibrate the WIRCam image using 2MASS objects, but this was not successful. We found that objects with sufficient signal-to-noise ratios in the 2MASS catalog are in the nonlinear regime of WIRCam. On the other hand, objects in the WIRCam linear regime are close to the detection limits of 2MASS where selection effects bias the 2MASS magnitudes. These make the calibration not better than 5%. Thus, we decided not to rely on 2MASS and instead calibrated the WIRCam image using our MOIRCS image (see §2.2.2), which was calibrated with frequent standard star observations.

The final WIRCam K_s -band mosaic covers an area of 30' \times 30'. Approximately 550 arcmin² has at least 10 hr of integration, and the deepest area has 39.7 hr of integration. The image FWHM is \sim 0''.8 and is quite uniform across the field. The rms astrometry error between the WIRCam catalog and the ACS/SuprimeCam reference catalog is 0''.13. The typical 5σ limiting magnitude in the 550 arcmin² deep area is $K_{s,AB} = 24.8$.

2.2.2. MOIRCS Imaging

MOIRCS contains two 2k \times 2k HAWAII2 detectors covering a field of view of \sim 4' \times 7' with a 0''.117 pixel scale. Our group and Japanese groups led by various investigators have imaged the ACS and *Spitzer* GOODS-N regions with multiple pointings in the K_s band. Part of the Japanese data were published in Kajisawa et al. (2006). Here we include all our data, taken between Dec 2005 and Jan 2008, and all the data available in the Subaru archive, taken between Jan 2005 and May 2006. The majority of the observations were performed under photometric conditions with excellent seeing of 0''.25 – 0''.6. A very small fraction of the data has large extinctions of > 0.5 mag or poor seeing of $> 0''.7$, and these observations were excluded

in this work.

The reduction of the MOIRCS images also used the SIMPLE package and is almost identical to the reduction of the WIRCam images described above. Here we only describe the differences. MOIRCS produces nearly circular fringes in roughly half of the images in K_s . The fringes were modeled in polar coordinates where they are almost straight lines and were subtracted from the images in the original Cartesian coordinates. The MOIRCS images were calibrated by observing various UKIRT Faint Standards (Hawarden et al. 2001) at least every half night on each detector. K_s band magnitudes of the standard stars were estimated by interpolating the H and K magnitudes in the UKIRT list assuming a power-law SED and using the H and K passbands for the UKIRT broadband filters and the MOIRCS K_s passband (see Tokunaga et al. 2002). Data taken under non-photometric conditions and poorly calibrated archive data were recalibrated with photometric data taken by our group.

The final MOIRCS K_s mosaic contains more than 20 pointings with different centers and position angles. The final mosaic has a total area of approximately 250 arcmin². Among all of the detected objects in the MOIRCS mosaic, the median 5σ limit is $K_{s,AB} = 24.85$, comparable to that of the WIRCam image. However, because of the different strategies adopted by the various groups, the MOIRCS coverage is extremely non-uniform. The deepest MOIRCS area is around the Hubble Deep Field-North (HDF-N) proper with a total integration time of \sim 22 hr and extremely deep 5σ limits of $K_{s,AB} = 26.2 - 26.7$. At some edges of the ACS and *Spitzer* GOODS-N regions the integration times are less than 20 min and the limiting magnitudes become < 23.9 . The MOIRCS mosaic has a very high image quality of 0''.4 – 0''.5 over the entire field of view. The rms astrometry error between the MOIRCS positions and the ACS/SuprimeCam reference catalog is 0''.08.

2.2.3. K_s catalog

We defined a sample of 6909 sources within the most uniformly covered ACS GOODS-N region (145 arcmin²) having $K_{s,AB} < 24.5$ in the WIRCam image, where $K_{s,AB}$ is a 3'' diameter aperture magnitude corrected to a 6'' diameter magnitude using a median offset measured for the brighter objects.

We list these sources in Table 1 ordered by K_s magnitude. We also give the flux and error from the WIRCAM image measured with the AUTO magnitude of SExtractor, which may provide a better approximation to the total magnitude for brighter galaxies in the sample. In constructing the catalog we eliminated a number of sources which lay within 3'' of a brighter object and where reliable photometry and spectroscopy could not be obtained. We also excluded objects that lay within an 8'' radius of the 9 brightest stars in the field for the same reason. We eliminated artifacts and fragments of larger galaxies by visual inspection of the images and by cross-comparing the independent MOIRCS and WIRCam data. In the table we give the catalog number (col. [1]), the right ascension and declination (col. [2]–[3]), the flux and 1σ error in μ Jy corresponding to the SExtractor AUTO magnitude (col. [4]–[5]), the K_s magnitude (col. [6]), the SExtractor AUTO magnitudes measured in the four ACS bands

(col. [7]–[10]), and the ground-based U -band magnitudes measured in a $3''$ diameter aperture and corrected to a $6''$ diameter magnitude using a median offset (col. [11]). We describe the remaining five columns of Table 1 in §3.

2.3. Mid-Infrared Imaging

We took as our primary MIR sample the DR1+ Multi-Band Imaging Photometer for *Spitzer* (MIPS; Rieke et al. 2004) $24\ \mu\text{m}$ source list of 1199 sources with fluxes above $80\ \mu\text{Jy}$ measured from the version 0.36 MIPS $24\ \mu\text{m}$ map of the *Spitzer* Legacy Program. This source list is a subset of a more extensive catalog which will be presented by R.-R. Chary et al. (2008, in preparation). The positions of corresponding *Spitzer* Infrared Array Camera (IRAC; Fazio et al. 2004) sources were used to measure the $24\ \mu\text{m}$ fluxes, where possible. We give this sample ordered by $24\ \mu\text{m}$ flux in Table 2. Assigning NIR and optical counterparts to the $24\ \mu\text{m}$ sources is complicated because of the uncertainties in the positions. We first applied the uniform offset of $-0'.4$ in declination to bring the absolute astrometry into the VLA frame. We next checked the relative astrometry by measuring the positions of the $24\ \mu\text{m}$ sources on the K_s images in cases where there was an unambiguous K_s counterpart. There appears to be a slight distortion in the $24\ \mu\text{m}$ astrometry relative to both the K_s image and the 20 cm image, but the effect is not large ($\lesssim 0'.5$ over the entire image). We used a linear fit to remove this. We then measured the position of the nearest K_s source. In most cases the counterpart is unambiguous; all but 65 of the sources have a K_s counterpart within $1''$. This reflects the use of the IRAC source positions as priors in generating the $24\ \mu\text{m}$ catalog. However, in some cases the $24\ \mu\text{m}$ source lies between two NIR galaxies, likely as a consequence of blending. In these cases we assigned the source to the nearest galaxy, or, in the most ambiguous cases, to the brightest nearby galaxy using the IRAC images, where available, or the K_s image otherwise. We give the initial position of each $24\ \mu\text{m}$ source (after astrometric correction) in columns (1) and (2) of Table 2, and we give the position of the adopted counterpart in columns (3) and (4). The 14 sources with separations greater than $1'.5$ from the counterpart are marked with the letter “w” after column (11). These counterparts should be treated with caution. The associated $24\ \mu\text{m}$ fluxes may be overestimated if the offset is a consequence of blending. We also list in Table 2 the $24\ \mu\text{m}$ flux (col. [5]), the K_s magnitude (col. [6]), and the four ACS magnitudes (cols. [7]–[10]). Where the object lies off the *HST* image, we give the z' , I , and B ground-based magnitudes instead (Capak et al. 2004). In these cases the F606W column is left blank. We give the U -band magnitude in column (11). We describe the remaining five columns of Table 2 in §3.

2.4. Near-Ultraviolet and Far-Ultraviolet Imaging

The Galaxy Evolution Explorer (GALEX) mission (Martin et al. 2005) obtained a deep 150 ks exposure of the ACS GOODS-N region in early 2004. We measured the near-ultraviolet (NUV; $2371\ \text{\AA}$ central wavelength) and far-ultraviolet (FUV; $1528\ \text{\AA}$ central wavelength) magnitudes from these images, which we obtained from the Multimission Archive at STScI (MAST). We used as a

prior the positions of the $F435W_{\text{AB}} = 26$ galaxy sample. Given the large point spread function ($4'.5\text{--}6''$ FWHM) of GALEX, we used an $8''$ diameter aperture to measure the magnitudes using the GALEX zeropoints of 20.08 for the NUV image and 18.82 for the FUV image. For the brighter objects ($F435W_{\text{AB}} = 20\text{--}23.5$ mag) we measured the median offset between the $8''$ magnitudes and the magnitudes that we measured in a $24''$ diameter aperture. We then used this to correct all of the $8''$ magnitudes to approximate total magnitudes. The magnitudes agree on average to within 0.05 mag with the SExtractor based magnitudes given in the GALEX NUV+FUV merged catalog for the region. We measured the noise level by randomly positioning apertures on blank areas of the sky and measuring the dispersion. We found 1σ limits of 26.8 for the NUV image and 27.4 for the FUV image.

GALEX has a large point-spread function, so contamination by neighbors is a serious problem. Thus, in generating an NUV+FUV sample of isolated galaxies, we eliminated sources which were closer than $8''$ to a brighter GALEX source at the same wavelength, or where, based on a visual inspection, the position was clearly contaminated by the wings of a nearby bright source. A substantial fraction of the galaxies in the optical sample are eliminated by this isolation requirement. The final sample contains 1016 sources with $\text{NUV}_{\text{AB}} < 25$ and 478 sources with $\text{FUV}_{\text{AB}} < 25.5$ (with considerable overlap between the two). We list these sources in Table 3 ordered by NUV magnitude. We give the right ascension and declination (cols. [1] and [2]), the NUV magnitude (col. [3]), and the FUV magnitude (col. [4]). Where we find a negative flux in the aperture, we show the magnitude corresponding to the absolute flux with a minus sign in front. We also give the $24\ \mu\text{m}$ flux (col. [5]), the K_s magnitude (col. [6]), the four ACS magnitudes (cols. [7]–[10]), and the U -band magnitude (col. [11]). We describe the remaining five columns of Table 3 in §3.

2.5. X-ray and Radio Imaging

Richards (2000) presented a catalog of 20 cm sources detected in the Very Large Array (VLA)¹⁰ map of the HDF-N, which covers a $40'$ diameter region with an effective resolution of $1.8''$. The absolute radio positions are known to $0.1''\text{--}0.2''$ rms. We cross-identified our catalogs with the radio catalog to obtain 20 cm fluxes.

Alexander et al. (2003) presented the 2 Ms X-ray image of the *Chandra* Deep Field-North (CDF-N), which they aligned with the Richards (2000) VLA image. Near the aim point the X-ray data reach limiting fluxes of $f_{2\text{--}8\ \text{keV}} \approx 1.4 \times 10^{-16}$ ergs $\text{cm}^{-2}\ \text{s}^{-1}$ and $f_{0.5\text{--}2\ \text{keV}} \approx 1.5 \times 10^{-17}$ ergs $\text{cm}^{-2}\ \text{s}^{-1}$. We use these data to identify AGNs, which we define on energetic grounds as any source more luminous than 10^{42} ergs s^{-1} (Zezas et al. 1998; Moran et al. 1999) calculated in either the rest-frame $0.5\text{--}2\ \text{keV}$ (soft) or rest-frame $2\text{--}8\ \text{keV}$ (hard) band. Trouille et al. (2008) present a table of redshifts for the full X-ray sample, including sources which lie outside the ACS or *Spitzer* GOODS-N regions.

3. THE SPECTROSCOPIC DATA

¹⁰The VLA is a facility of the NRAO.

Our primary goal for this paper was to obtain the most complete and homogeneous spectral database possible for the GOODS-N field. Over the years a number of groups have made observations of this region, first primarily using the Low-Resolution Imaging Spectrograph (LRIS; Oke et al. 1995) on the Keck I telescope (these data are summarized in Cohen et al. 2000), and later using the large-format Deep Extragalactic Imaging Multi-Object Spectrograph (DEIMOS; Faber et al. 2003) on the Keck II 10 m telescope. Wirth et al. (2004; Team Keck Treasury Redshift Survey or TKRS) and Cowie et al. (2004) presented large samples of magnitude-selected redshifts obtained using DEIMOS. In addition, Reddy et al. (2006) gave a substantial sample of color-selected redshifts, Chapman et al. (2004, 2005) and Swinbank et al. (2004) presented a small number of radio/submillimeter redshifts, and Treu et al. (2005) measured redshifts for a sample of spheroids. Barger et al. (2003), Trouille et al. (2008), and Barger et al. (2007) carried out extensive observations of the X-ray and 20 cm sources in the CDF-N.

Here we have added to these samples by observing all of the missing or unidentified galaxies in the F435W, F850LP, K_s , and 24 μm selected samples. In order to provide a uniform spectral database, we also reobserved sources where the original spectra were of poor quality or where previous redshifts were obtained with instruments other than DEIMOS, as well as where the existing redshift identifications were unconvincing (a small number).

We made our observations over a number of DEIMOS runs between 2004 and 2007. We used the 600 lines per mm grating, giving a resolution of 3.5 \AA and a wavelength coverage of 5300 \AA , which was also the configuration used in the TKRS observations. The spectra were centered at an average wavelength of 7200 \AA , though the exact wavelength range for each spectrum depends on the slit position. Each ~ 1 hr exposure was broken into three subsets, with the objects stepped along the slit by $1''.5$ in each direction. Unidentified sources were continuously reobserved giving maximum exposure times of up to 7 hr. The spectra were reduced in the same way as previous LRIS spectra (Cowie et al. 1996). Only spectra that could be confidently identified based on multiple emission and/or absorption lines were included in the sample. A number of spectra were identified based on the doublet structure of the [OII] 3727 \AA line, which is resolved in the spectra.

In Table 4 we list the redshifts for 2907 sources in the ACS GOODS-N field. Only sources with $K_{s,AB} < 24.5$ or $F850LP_{AB} < 26$ are included, which omits a small number of emission line galaxies with known redshifts in the area. (A table of emission line galaxies will be given in E. M. Hu et al. 2008, in preparation.) The table is ordered by right ascension. We give the right ascension and declination (cols. [1] and [2]), the K_s , F850LP, F775W, F606W, F435W, and U magnitudes (cols. [3]–[8]), the spectroscopic redshift (col. [9]), the source of the redshift (col. [10]; see Table 6), the 24 μm flux in μJy (col. [11]), and the rest-frame 2–8 keV (col. [12]) and 0.5–2 keV (col. [13]) X-ray luminosities in units of 10^{40} ergs s^{-1} . Four stars were classified primarily on compactness and on their unambiguous stellar colors. These are shown without a source number in the tables and may be removed if desired.

We summarize the fraction of spectroscopically identified objects as a function of color and magnitude in

Table 5. The redshift identifications are greater than 90% complete to magnitudes of $F435W_{AB} = 24.5$, $F850LP_{AB} = 23.3$, and $K_{s,AB} = 21.5$.

In Table 6 we list the published catalogs (the journal references are given in col. [5]) that we used in assembling our various redshift tables. We have assigned a unique source number (col. [1]) to each catalog. It is this source number which appears in column (10) of Table 4. We also summarize in Table 6 the number of redshifts present in each catalog (col. [2]) and the number of redshifts that appear only in that catalog (“unique”, col. [3]). We give a cumulative redshift count of all the identified galaxies in column (4). Galaxies from sources 1 and 2 have uniform DEIMOS spectra, while galaxies from source 3 have LRIS spectra. The galaxies from these three sources form our *spectral* database.

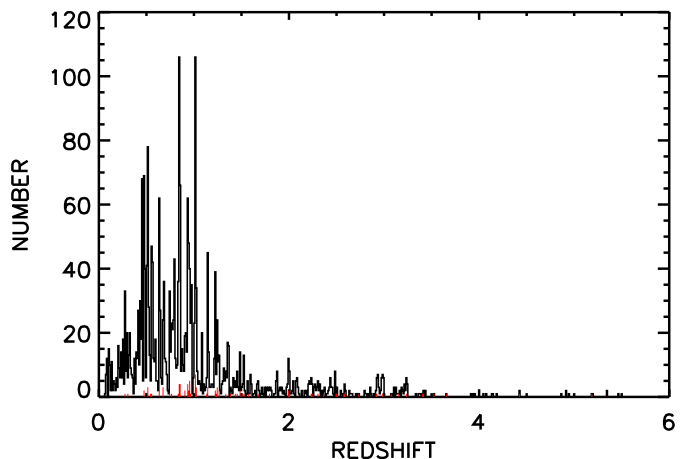


FIG. 1.— Redshift distribution of the sources in Table 4. The bin size is 0.01. AGNs are shown in red.

We show the redshift distribution in Figure 1. Most of the redshifts are at $z < 1.6$ (2362 sources) where the [OII] 3727 \AA line still lies in the DEIMOS spectroscopic range, 327 lie between $z = 1.6 - 3.5$, mostly from the LRIS observations of Reddy et al. (2006), and there are relatively few objects (only 21) with spectroscopic redshifts $z > 3.5$. In total, 98 of the objects are classified as containing AGNs that could be significant contributors to the galaxy light based on either their rest-frame hard or soft X-ray luminosities being above 10^{42} ergs s^{-1} . We show on the figure the redshift distribution for these AGNs (*red*).

We also list the spectroscopic redshifts for the $K_{s,AB} < 24.5$ sample as a function of K_s magnitude in Table 1 (col. [12]; there are redshifts for 2596 stars and galaxies in this sample), for the 24 μm sample as a function of 24 μm flux in Table 2 (col. [12]; the *Spitzer* area covered is larger than the area covered by the optical/NIR catalog, so 213 of the 743 galaxies and stars with spectroscopic identifications in this sample lie outside the ACS area), and for the NUV+FUV sample as a function of NUV magnitude in Table 3 (col [12]).

The remaining columns in Table 1 are the source of the redshift (col. [13]), the 24 μm flux in μJy (col. [14]), and the rest-frame 2–8 keV (col. [15]) and 0.5–2 keV (col. [16]) X-ray luminosities in units of 10^{40} ergs s^{-1} . The remaining columns in Table 2 and Table 3 are the source of the redshift (col. [13]), the rest-frame 2–8 keV (col. [14]) and 0.5–2 keV (col. [15]) X-ray luminosities in units of

10^{40} ergs s^{-1} , and the 20 cm flux in μJy (col. [16]).

In Figure 2 we show redshift versus 24 μm flux for the 80 μJy MIR sample. We use red large squares to denote AGNs with rest-frame hard or soft X-ray luminosities in excess of 10^{42} ergs s^{-1} . At the base of the plot we show a histogram of the fraction of sources per half magnitude bin that remain spectroscopically unidentified. The sample is essentially complete to 500 μJy .

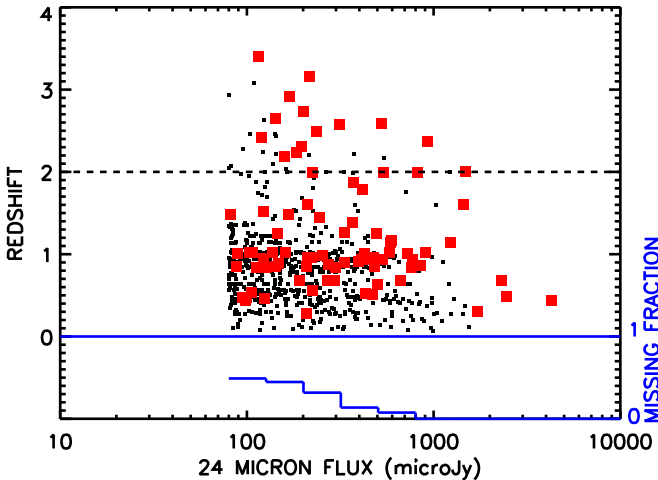


FIG. 2.— Redshift vs. 24 μm flux for the 80 μJy MIR sample. AGNs, defined as sources with rest-frame hard or soft X-ray luminosities $> 10^{42}$ ergs s^{-1} , are denoted by red large squares. The fraction of unidentified sources per 0.5 mag bin is shown in histogram form at the bottom of the plot (label is on right-hand y-axis). The dashed horizontal line shows $z = 2$.

In Figure 3 we show redshift-magnitude diagrams for the (a) $FUV_{AB} < 25$, (b) $NUV_{AB} < 25$, and (c) $U_{AB} < 25$ samples. In each panel we show the redshift at which the Lyman continuum break passes through the center of the filter (*dashed horizontal lines*; i.e., $z = 0.67$, $z = 1.6$, and $z = 3.06$, respectively, for the FUV, NUV, and U -band filters). The sharp cut-offs above these redshifts are clearly seen, and, perhaps surprisingly, apply to both the AGNs (*red large squares*) and the galaxies, with very few sources in either category lying above the cut-offs. We shall return to this point when we consider LBG selection in §4.1. In Figure 4 we show redshift-magnitude diagrams for the (a) $F435W_{AB} < 25$, (b) $F606W_{AB} < 24$, (c) $F850LP_{AB} < 24$, and (d) $K_{s,AB} < 23$ samples.

4. COLOR SELECTION TECHNIQUES

We use the spectroscopic sample to test three color selection techniques that can be used to pick out galaxies in a given redshift range: the LBG dropout technique, the BzK color selection, and the H^- method in the MIR. For each method there are two quantities of interest. (1) If one were to use the method to select galaxies in the given redshift range for spectroscopic follow-up or for direct analysis, then the first quantity of interest is the fraction of objects which lie outside the redshift range that are found by the selection. We will call this the selection contamination. (2) The second quantity of interest is the fraction of objects which lie in the redshift range that are actually found by the color selection. We will call this the selection completeness.

In general the color selections are tuned to provide a reasonable balance between selection contamination and se-

lection completeness and can be adjusted to optimize one or the other. Thus, if one were using the color selection to choose objects for spectroscopic follow-up, a high level of contamination might be acceptable in order to make sure the sample contained most of the objects in the redshift range. On the other hand, if the primary goal were to choose a set of objects in the redshift range based on colors, then one might want to minimize contamination even if one missed a number of objects in the redshift range.

4.1. The LBG Selection

In Figure 5 we show the $2.7 \leq z \leq 3.4$ LBG color-color selection (*blue solid lines*) for our 98.4% spectroscopically complete $F606W_{AB} < 23.5$ sample. This sample consists of 1197 galaxies and stars, only 18 of which are not identified. Our selection is

$$(U - F606W)_{AB} > 1.2 \quad (1)$$

$$\text{for } (F606W - F850LP)_{AB} \leq 0.25,$$

and

$$(U - F606W)_{AB} > (F606W - F850LP)_{AB} \times 2.4 + 0.6 \quad (2)$$

$$\text{for } 0.25 < (F606W - F850LP)_{AB} < 0.8.$$

Using the SExtractor stellarity index, as measured in the ACS F850LP image, we have divided the sample into extended (< 0.5 ; Fig. 5a) and compact (> 0.5 ; Fig. 5b) sources (*black diamonds for $z \leq 2.7$ galaxies; red upside-down triangles for $z > 2.7$ galaxies; purple stars for spectroscopically identified stars; green triangles for unidentified sources*). We denote the AGNs (rest-frame hard or soft X-ray luminosities $> 10^{42}$ ergs s^{-1}) with large squares (*blue for $z \leq 2.7$; red for $z > 2.7$*). We enclose in larger black squares those AGNs classified as broad-line AGNs, and we enclose in larger black diamonds those AGNs with high-excitation emission lines (C IV or [Ne V]).

The LBG selection works well for the one $z > 2.7$ galaxy (high selection completeness). This object is cleanly picked out at these magnitudes (Fig. 5a). Additionally, only a small number of other sources cross the boundary in either Figure 5a or Figure 5b (modest selection contamination). However, the three $z > 2.7$ AGNs are not picked out by the LBG selection, though they do lie close to the boundary. This is reasonable for the two compact $z > 2.7$ AGNs in Figure 5b. Both show AGN signatures in their optical spectra, and the dominant AGN light would not be expected to have a strong Lyman break. However, the $z > 2.7$ AGN in Figure 5a shows no AGN signatures in its optical spectrum, and it is dominated by the extended galaxy light. It would not be classified as an AGN based on its optical spectrum, which shows strong UV absorption lines and very weak $Ly\alpha$ emission. It appears that the AGN is weakening the break signature and dropping the object from the LBG selection while not dominating the longer wavelength light.

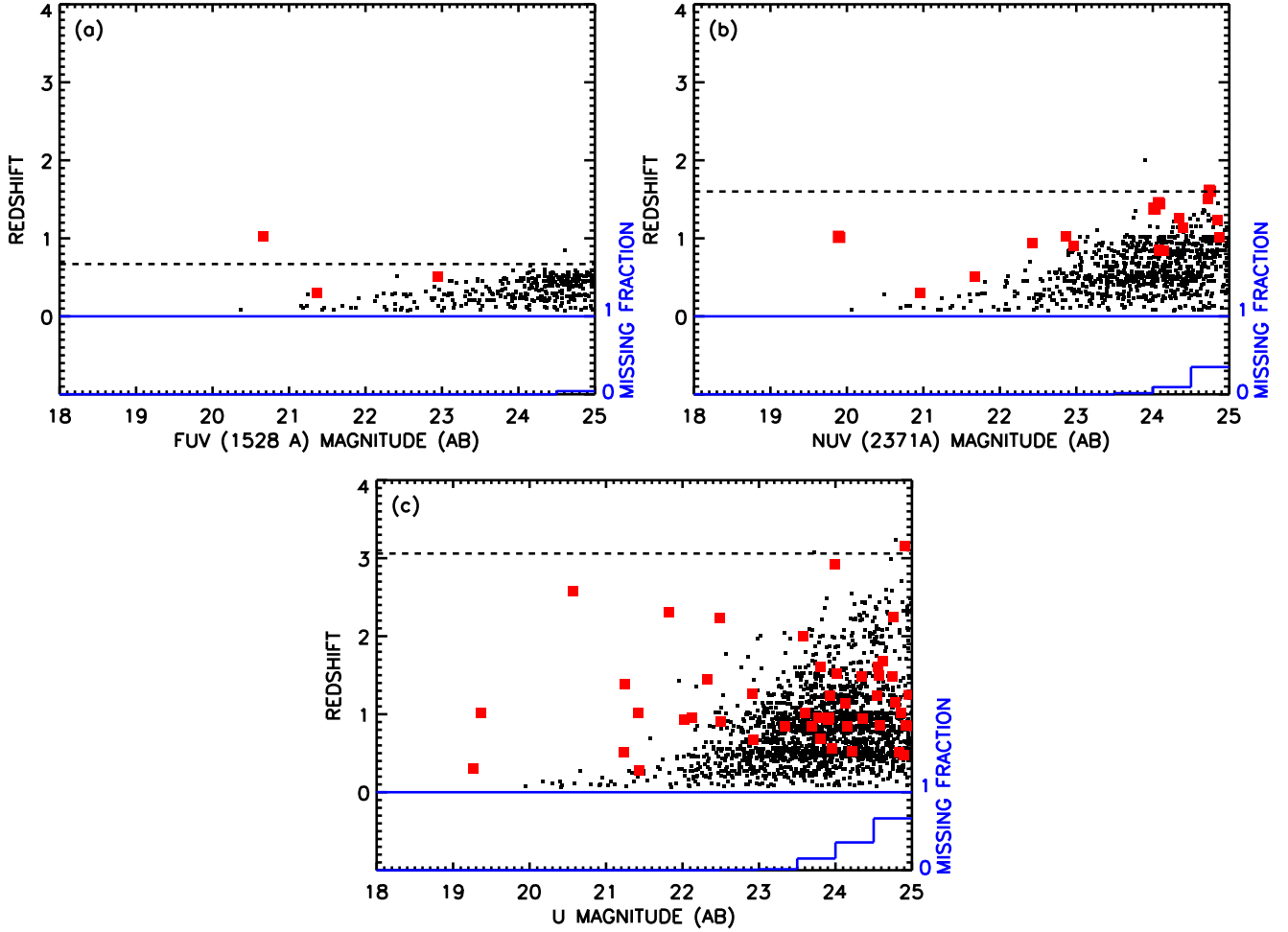


FIG. 3.— Redshift vs. (a) FUV_{AB} magnitude for the $FUV_{AB} < 25$ sample, (b) NUV_{AB} magnitude for the $NUV_{AB} < 25$ sample, and (c) U_{AB} magnitude for the $U_{AB} < 25$ sample. AGNs, defined as sources with rest-frame hard or soft X-ray luminosities $> 10^{42}$ ergs s^{-1} , are denoted by red large squares. The dashed horizontal lines show the redshifts at which the Lyman continuum break passes through the center of each filter: (a) $z = 0.67$ for the FUV, (b) $z = 1.6$ for the NUV, and (c) $z = 3.06$ for the U -band. The fraction of unidentified sources per 0.5 mag bin is shown in histogram form at the bottom of each plot (label is on the right-hand y-axis).

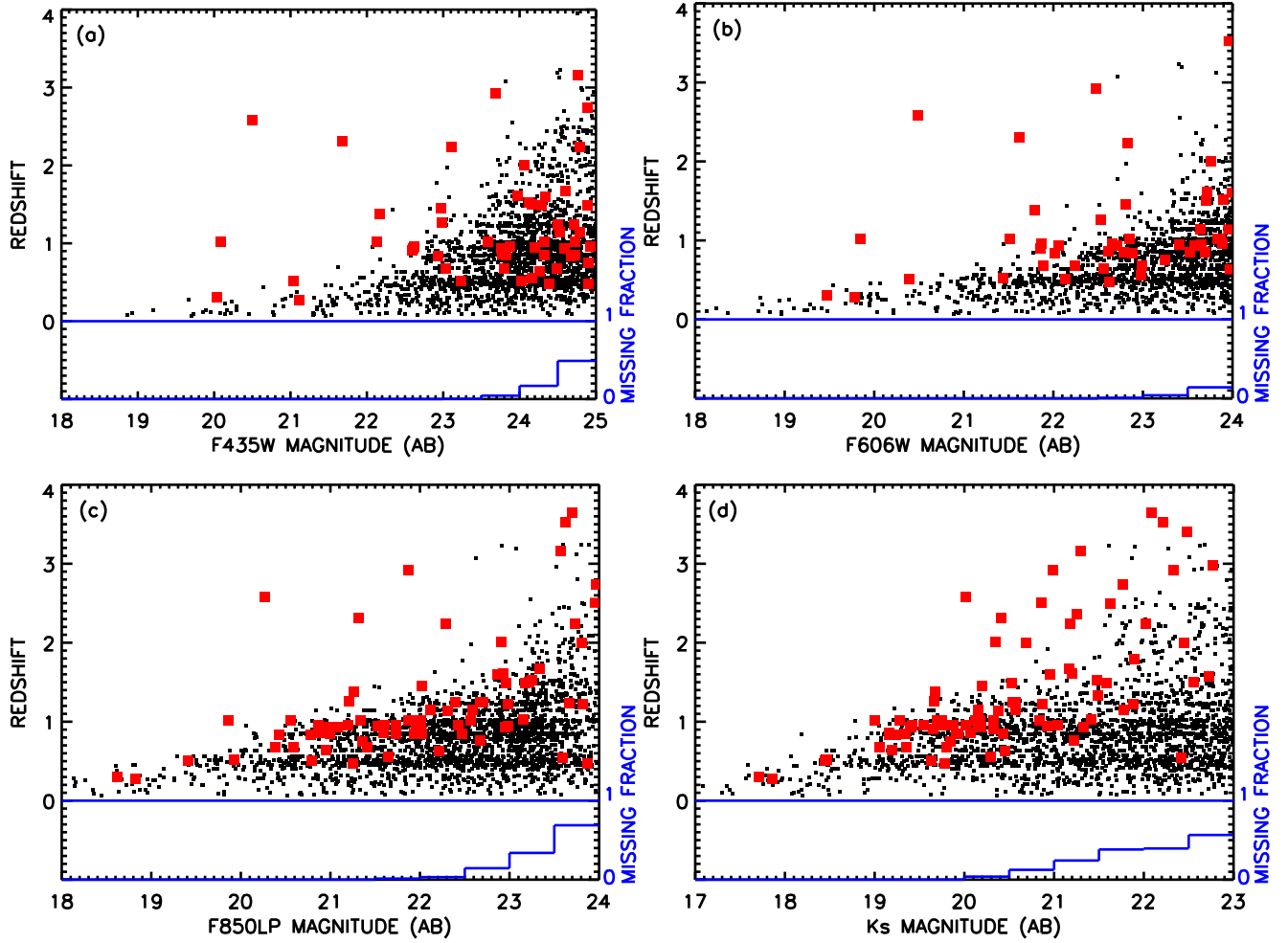


FIG. 4.— Redshift vs. (a) $F435W_{AB}$ magnitude for the $F435W_{AB} < 25$ sample, (b) $F606W_{AB}$ magnitude for the $F606W_{AB} < 24$ sample, (c) $F850LP_{AB}$ magnitude for the $F850LP_{AB} < 24$ sample, and (d) $K_{s,AB}$ magnitude for the $K_{s,AB} < 23$ sample. AGNs, defined as sources with rest-frame hard or soft X-ray luminosities $> 10^{42}$ ergs s^{-1} , are denoted by red large squares. The fraction of unidentified sources per 0.5 mag bin is shown in histogram form at the bottom of each plot (label is on the right-hand y-axis).

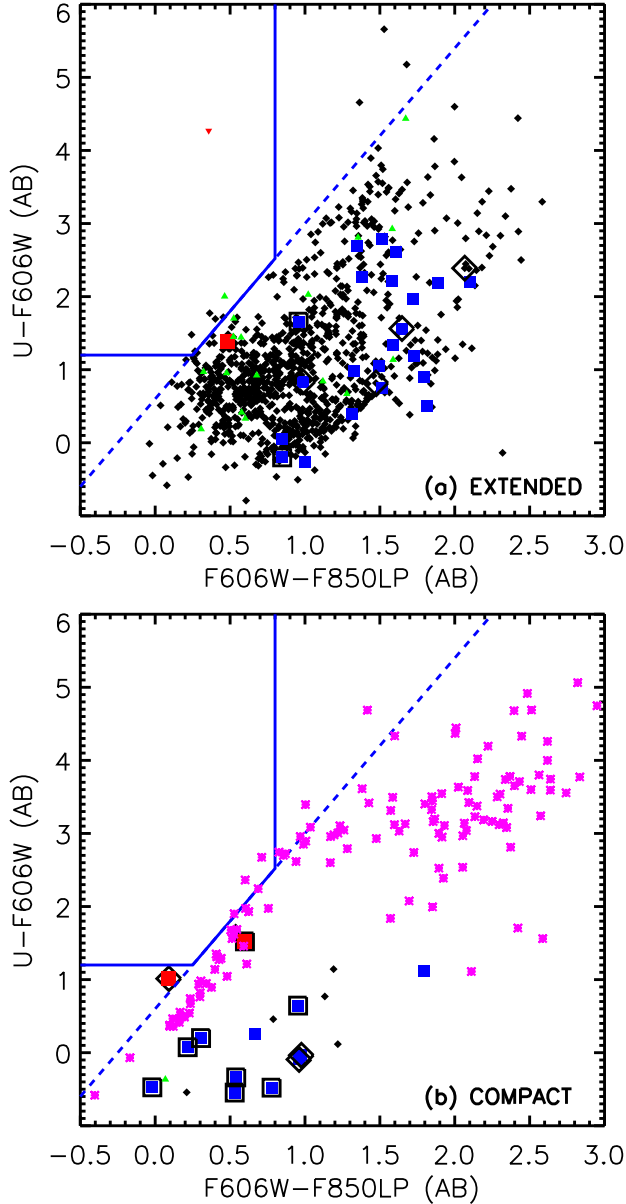


FIG. 5.— $(U - F606W)_{AB}$ vs. $(F606W - F850LP)_{AB}$ color-color diagram for our nearly spectroscopically complete $F606W_{AB} < 23.5$ sample (black diamonds for $z \leq 2.7$ galaxies; red upside-down triangles for $z > 2.7$ galaxies; purple stars for spectroscopically identified stars; green triangles for unidentified sources), divided into (a) extended and (b) compact sources, depending on whether the SExtractor stellerity index in the ACS F850LP image is less than or greater than 0.5, respectively. All of the spectroscopically identified stars fall in (b). The large squares are AGNs (blue for $z \leq 2.7$; red for $z > 2.7$). Those AGNs classified as broad-line AGNs are enclosed in larger black squares, and those with high-excitation emission lines (C IV or [Ne V]) are enclosed in larger black diamonds. The blue solid lines mark where LBGs with $2.7 \leq z \leq 3.4$ would be searched for in a color-color pre-selection.

We show the break selection in a different way in Figure 6, where we plot a U break parameter versus redshift in three magnitude intervals for every $F850LP_{AB} \geq 19$ source with a measured spectroscopic redshift. We define the U break parameter to be

$$(U - F606W)_{AB} - (F606W - F850LP)_{AB} \times 2.4 - 0.6. \quad (3)$$

This is just a measure of how far above or below the diagonal selection limit (blue dashed line in Fig. 5) each galaxy

lies. We also show the colors of a few Bruzual & Charlot (2003) model tracks, illustrating that the break parameter passes through zero at $z = 2.7$ for a wide range of galaxy types.

We have divided the sources into three magnitude ranges: (a) $19 \leq F606W_{AB} < 22.75$, where all but one of the galaxies (with $F606W_{AB} = 22.69$) are identified, (b) $22.75 \leq F606W_{AB} < 23.5$, where the galaxy identifications are 97% complete, and (c) $23.5 \leq F606W_{AB} < 24.5$, where a substantial number of $z > 2.7$ galaxies enter the sample. The galaxies follow a remarkably well-defined track in all the panels. In Figure 6a only the two AGNs have $z > 2.7$ and, as we have discussed above, both lie close to the zero U break parameter. In Figure 6b we see the appearance of the first $z > 2.7$ galaxy, which has a magnitude of $F606W_{AB} = 23.4$. This galaxy lies above the selection limit, while the extended galaxy+AGN discussed above, which also appears in this figure, does not.

In Figure 6c the $z = 2.7 - 3.4$ sources become more common. Twelve lie above the selection limit and five lie below, of which only two lie fairly far below, including one further extended source with a weak AGN. Of particular note is the relatively small number of sources in the lower-right quadrant in all three panels. This is not consistent with the work of Le Fèvre et al. (2005) and Paltani et al. (2007), who claim to have discovered a significantly larger galaxy population at high redshifts ($z \sim 3$) than had previously been identified, particularly at bright magnitudes. They found that their $2.7 \leq z \leq 3.4$ galaxies were mainly located near the boundary used to isolate LBGs in their $u-g, g-r$ color-color diagram, so they adopted a very conservative diagonal limit for their selection criterion at the expense of more contamination from low-redshift galaxies. We find no evidence for a strong population of this type of galaxy.

We can perform a similar analysis at lower redshifts using the GALEX magnitudes. In Figures 7a and 7c we show the LBG selection of $0.6 \leq z < 1.4$ galaxies (blue solid lines) using the $(FUV - NUV)_{AB}$ vs. $(NUV - F435W)_{AB}$ color-color diagram. In Figures 7b and 7d we show the selection of $1.4 \leq z < 2.7$ galaxies (blue solid lines) using the $(NUV - U)_{AB}$ vs. $(U - F606W)_{AB}$ color-color diagram. In both cases we have used an equivalent selection to that of the high-redshift LBGs. For Figures 7a and 7c we include all sources with $NUV_{AB} < 23.75$, which is 100% spectroscopically complete. For Figures 7b and 7d we include all sources with $U_{AB} < 23.75$, which is 97% spectroscopically complete. An $NUV_{AB} = 23.75$ magnitude limit at $z = 1$ corresponds to an $F606W$ limit of 26 at $z = 3$, so these near-ultraviolet samples extend to much lower luminosities than the $F606W$ sample. The samples have been divided into extended (< 0.5 ; Figs. 7a and 7b) and compact (> 0.5 ; Figs. 7c and 7d) using the SExtractor stellerity index, as measured in the ACS F850LP image.

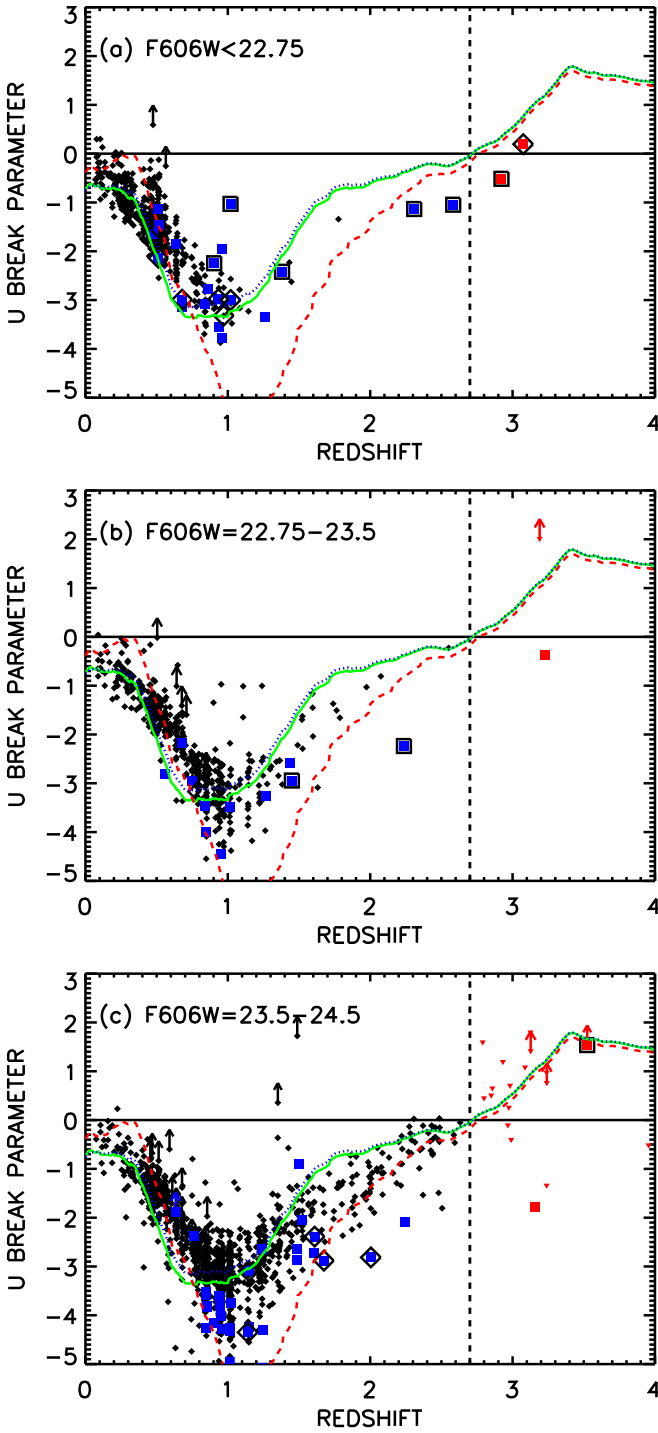


FIG. 6.— U break parameter $[(U - F606W)_{AB} - (F606W - F850LP)_{AB} \times 2.4 - 0.6]$ vs. redshift for every $F850LP_{AB} \geq 19$ galaxy with a spectroscopic redshift (black for $z \leq 2.7$; red for $z > 2.7$). The large squares are AGNs (blue for $z \leq 2.7$; red for $z > 2.7$). The broad-line AGNs are shown enclosed in larger black squares. Sources with high-excitation emission lines (C IV or [Ne V]) are shown enclosed in larger black diamonds. The arrows show 2σ lower limits. (a) $19 \leq F606W_{AB} < 22.75$, where every galaxy has a spectroscopic redshift; (b) $22.75 \leq F606W_{AB} < 23.5$, where 97% of the galaxies have redshifts and where there is only one $z > 2.7$ galaxy; and (c) $23.5 \leq F606W_{AB} < 24.5$, where $z > 2.7$ sources begin to appear in significant numbers. The dashed vertical line marks the $z = 2.7$ lower limit of the LBG redshift selection. The curves show the expected break parameters from Bruzual & Charlot (2003) models for exponentially declining star formation rates with decline times of 10^9 yrs (red dashed), 5×10^9 yrs (green solid), and 10^{10} yrs (blue dotted), solar metallicities, and ages equal to the age of the universe at that redshift.

The color-color diagrams pick out nearly all of the galaxies above the selection limits ($z > 0.6$ or $z > 1.4$). Figures 7a and 7c suggest that the $(NUV - F435W)_{AB}$ constraint could be relaxed without increasing the selection contamination. It can be seen from Figures 5 and 6 that the vertical constraint can also be relaxed at higher redshifts, except as a way to minimize the star contamination problem when the LBG selection is applied without a compactness measurement. (Figure 5b shows how the star track edges into the selection region; some of these can be eliminated by the $[F606W - F850LP]_{AB} < 0.8$ constraint.) From Figure 7d we see that star contamination can be substantial if we use the LBG method to select $z \sim 1$ galaxies without compactness information.

The color selections in Figure 7 are also surprisingly good at picking out AGNs, including many of the broad-line AGNs, suggesting that some of these have strong Lyman breaks also. However, as with the high-redshift sample, there are AGNs which would be missed by the color selection. Cowie et al. (2008) discusses the implications of this for the production of the metagalactic ionizing flux.

We may use the 100% complete $NUV_{AB} < 23.75$ sample of Figures 7a and 7c to assess the selection completeness and the selection contamination. Of the 86 galaxies in that sample with $z > 0.6$, 79 are selected by the cuts

$$(FUV - NUV)_{AB} > 1.2, \quad (4)$$

and

$$(FUV - NUV)_{AB} > (NUV - U)_{AB} \times 2.4 + 0.6. \quad (5)$$

This gives a selection completeness of 92%. Note that one of the seven omitted sources is an X-ray luminous broad-line quasar, and one is an AGN with high-excitation lines. Since the above cuts pick out 116 sources, the selection contamination by sources with $z \leq 0.6$ is 32%.

We conclude that while there may be a very small number of unusual sources where AGN contamination (or some other cause) moves the source outside the selection region, more than 90% of galaxies in the desired redshift range will be picked out by the LBG selection. While we have based our analysis on the low-redshift sample, the selection completeness should only be higher at high-redshifts, where the effects of the Ly α forest accentuate the LBG selection.

4.2. The BzK Selection

Daddi et al. (2004) proposed a NIR selection technique for finding high-redshift galaxies defined by

$$BzK \equiv (z - K_s)_{AB} - (B - z)_{AB}. \quad (6)$$

With this relation, $z > 1.4$ star-forming galaxies can be identified using the criterion $BzK \geq -0.2$, while $z > 1.4$ old stellar systems can be isolated using the criteria $BzK < -0.2$ and $(z - K_s)_{AB} > 2.5$. Daddi et al. (2004) applied the technique to the K20 ($K_{s,AB} < 21.8$) survey (Cimatti et al. 2002). This survey includes a 32 arcmin² region in the GOODS-S, where 328 of the 347 sources have spectroscopic redshifts, and a 19 arcmin² area centered on the QSO 0055-269 at $z = 3.656$, where 176 of the 198 sources have spectroscopic redshifts. They also

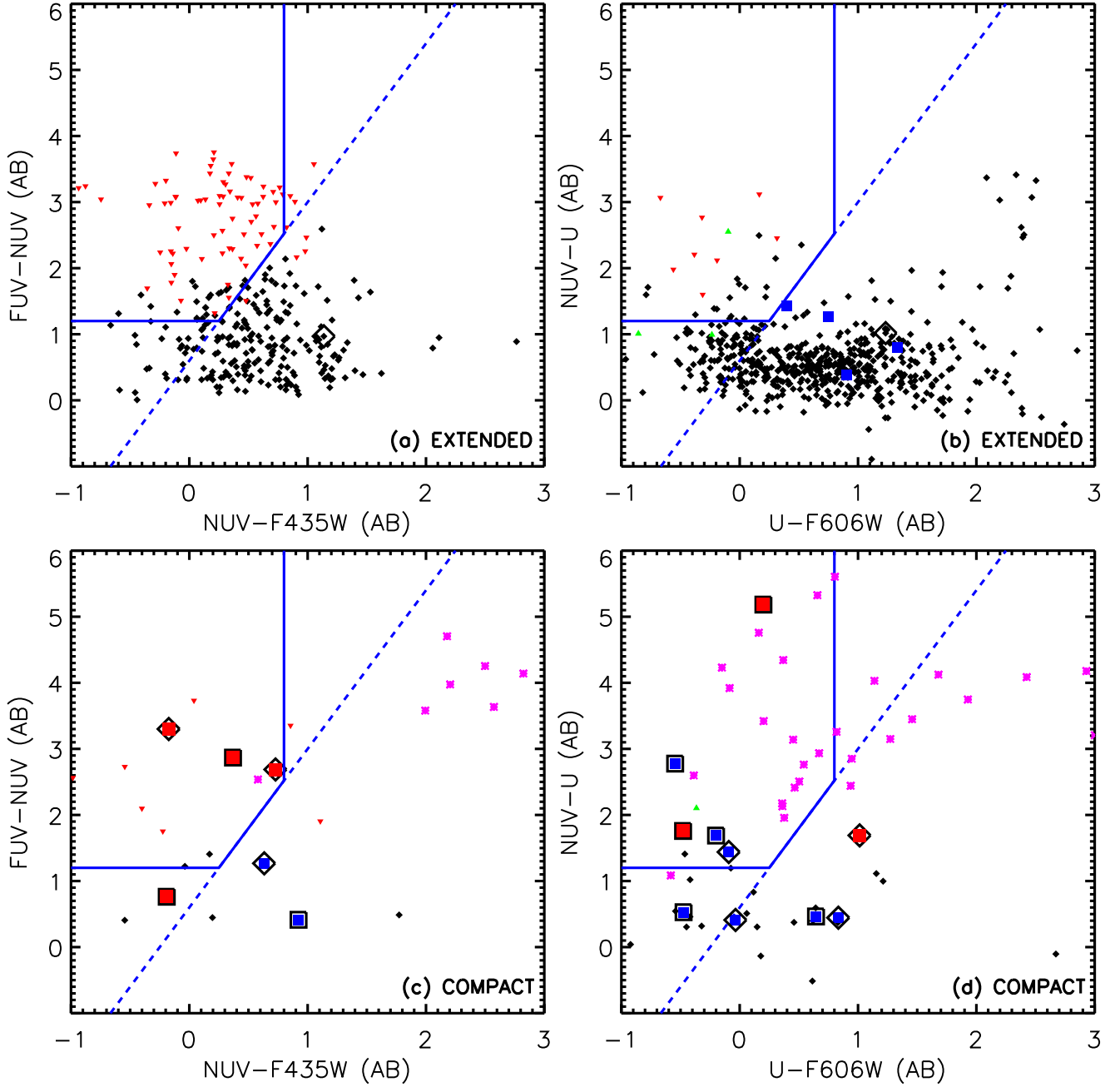


FIG. 7.— (a) Extended and (c) compact $(FUV-NUV)_{AB}$ vs. $(NUV-F435W)_{AB}$ and (b) extended and (d) compact $(NUV-U)_{AB}$ vs. $(U-F606W)_{AB}$ color-color diagrams for our 100% spectroscopically complete $NUV_{AB} < 23.75$ sample (a and c) and our 97% spectroscopically complete $U_{AB} < 23.75$ sample (b and d). The extended and compact designations depend on whether the SExtractor stellarity index in the ACS F850LP image is less than or greater than 0.5, respectively. In (a) and (c) the black diamonds are galaxies with spectroscopic redshifts $z \leq 0.6$, the red upside-down triangles are galaxies with spectroscopic redshifts $z > 0.6$, the large squares are AGNs (*blue for $z \leq 0.6$; red for $z > 0.6$*), and the blue solid lines mark where LBGs with $z > 0.6$ would be searched for in a color-color pre-selection. In (b) and (d) the black diamonds are galaxies with spectroscopic redshifts $z \leq 1.4$, the red upside-down triangles are galaxies with spectroscopic redshifts $z > 1.4$, the large squares are AGNs (*blue for $z \leq 1.4$; red for $z > 1.4$*), the blue solid lines mark where LBGs with $z > 1.4$ would be searched for in a color-color pre-selection, and the green triangles are the unidentified sources. All of the spectroscopically identified stars (*purple stars*) fall in the compact panels. In all panels the broad-line AGNs are shown enclosed in larger black squares, and sources with high-excitation emission lines (C IV or [Ne V]) are shown enclosed in larger black diamonds.

utilized photometric redshifts, which make up a sizeable fraction of their $z > 1.4$ sample. Daddi et al. (2004) found that their BzK selection criteria did very well at selecting $z > 1.4$ galaxies; moreover, only about 12% of their final sample were lower redshift “interlopers”. Some of this contamination was due to AGNs. They also checked their criteria on two deeper samples, a spectroscopic sample to $K_{s,AB} = 22.4$ from the Gemini Deep Deep Survey (GDDS; Abraham et al. 2004) and a photometric sample to $K_{s,AB} = 23.8$ from ISAAC imaging of the same GOODS-S region covered by the K20 survey. These samples supported the continued validity of the method for magnitudes fainter than $K_{s,AB} = 21.8$, though the GDDS sample of $z > 1.4$ galaxies was small, and the ISAAC sample did not have spectroscopic redshifts. (Popesso et al. 2008 have since increased the number of spectroscopic redshifts in the GOODS-S field using VIMOS. However, it does not appear that they are using a K_s selected sample in their Figure 10 BzK diagram.)

Because it is important to understand how well the BzK selection works, especially before applying the method to extremely large samples, such as those being generated by the UKIRT Infrared Deep Sky Survey (UKIDSS; Lane et al. 2007), several other groups have also tried to test its reliability. In most of these cases the authors have compared the locations of the sources in the BzK diagram with their photometric redshift estimates (e.g., Kong et al. 2006; Grazian et al. 2007; Quadri et al. 2007). However, the difficulty with this approach is that the colors used to construct the BzK diagram and the photometric redshift estimates are not independent.

4.2.1. Our Nearly Spectroscopically Complete Sample

We can investigate the reliability of the BzK method using our nearly complete, large spectroscopic sample in the GOODS-N region. The area covered by our sample is substantially larger than that of the K20 survey (145 arcmin² versus 51 arcmin²), though the $K_{s,AB}$ limit to which we are complete to the same level as K20 is shallower ($K_{s,AB} = 21.4$ versus $K_{s,AB} = 21.8$).

In Figure 8 we restrict our sample to the magnitude range $15 < K_{s,AB} \leq 21$ (the lower limit is to avoid saturation problems, which would lead to incorrect colors). Out of the 964 sources in this sample, only 45 have not been spectroscopically identified (*green triangles*). We use red symbols (*upside-down triangles for galaxies and red large squares for AGNs*) to show the $z > 1.4$ sources, and we use black diamonds for galaxies and blue large squares for AGNs to show the $z \leq 1.4$ sources. We denote the spectroscopically identified stars with purple star symbols, and we use purple large open squares to show sources whose SExtractor stellerity index, as measured in the F850LP image, is > 0.5 (i.e., compact). This parameter identifies all of the spectroscopic stars and many of the AGNs as compact sources. We see a very tight sequence for the $z \leq 1.4$ galaxies. We also see that the BzK criterion (*diagonal line*) does a reasonable job of separating most of the sources into the correct redshift regimes. However, we note that to this magnitude limit only one spectroscopically identified galaxy at $z > 1.4$ lies in the passive galaxies region of the diagram (to the right of the diagonal line and above the horizontal line).

There are 15 spectroscopically identified $z > 1.4$ sources

to the left of the diagonal line and only three (one of which lies in the $z > 1.4$ passive galaxy region) to the right of the diagonal line. Thus, the BzK selection of $z > 1.4$ star-forming galaxies (i.e., excluding the $z > 1.4$ source in the passive galaxy region) has a high selection completeness (88%).

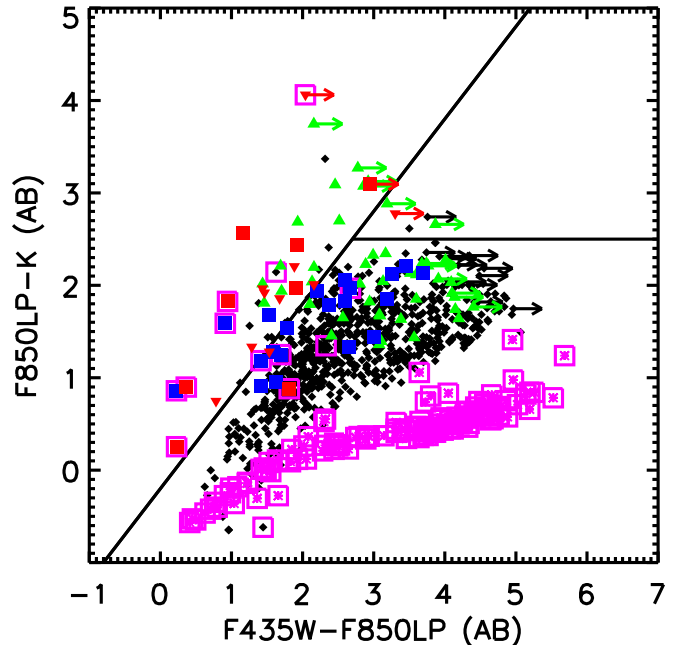


FIG. 8.— $(F850LP - K)_{AB}$ vs. $(F435W - F850LP)_{AB}$ for the $15 < K_{s,AB} \leq 21$ sample. The $z \leq 1.4$ galaxies are denoted by black diamonds, and the $z > 1.4$ galaxies are denoted by red upside-down triangles. AGNs are denoted by large squares (*blue for $z \leq 1.4$; red for $z > 1.4$*). The unidentified sources are denoted by green triangles. Sources with only 2σ lower limits in F435W are denoted by right-pointing arrows. Spectroscopically identified stars are denoted by purple star symbols. The purple large open squares show sources whose SExtractor stellerity index measured on the F850LP image is > 0.5 . The black diagonal line shows the $BzK \geq -0.2$ selection of $z > 1.4$ star-forming galaxies. This line combined with the horizontal line shows the $F850LP - K_s > 2.5$ selection of old galaxies at $z > 1.4$. Both were proposed by Daddi et al. (2004).

We can also estimate the minimum and maximum selection contamination by taking into account the 45 spectroscopically unidentified sources in the sample. 13 of these lie in the $z > 1.4$ star-forming region, 2 in the $z > 1.4$ passive galaxies region, and the remaining 30 in the $z \leq 1.4$ region.

We first consider the $z \leq 1.4$ region of the diagram. Here there are two spectroscopically identified $z > 1.4$ sources (interlopers) and 768 spectroscopically identified $z \leq 1.4$ sources. If we assume that all 30 of the unidentified sources in the $z \leq 1.4$ region do in fact have $z \leq 1.4$, then we obtain a minimum selection contamination of 0.25%. If we instead assume that all 30 of the unidentified sources in the $z \leq 1.4$ region actually have $z > 1.4$ (interlopers), then we obtain a maximum selection contamination of 4%.

We next consider the $z > 1.4$ star-forming region of the diagram (i.e., we are not considering the $z > 1.4$ passive region). Here there are 14 spectroscopically identified $z \leq 1.4$ sources (interlopers) and 15 spectroscopically identified $z > 1.4$ sources. If we assume that all 13 of the unidentified sources in the $z > 1.4$ star-forming region do in fact have $z > 1.4$, then we obtain a minimum selection contamination of 33%. If we instead assume that all 13

of the unidentified sources in the $z > 1.4$ star-forming region actually have $z \leq 1.4$ (interlopers), then we obtain a maximum selection contamination of 64%.

We conclude that at these magnitudes the BzK selection of $z > 1.4$ star-forming galaxies has a high selection completeness but a substantial selection contamination. Thus, BzK is effective at picking out high-redshift candidates, but spectroscopic follow-up is crucial to weed out the substantial number of interlopers.

4.2.2. Our Fainter Magnitude Sample

It is important to try to push the BzK analysis to fainter magnitudes, even with the increasing spectroscopic incompleteness. Reddy et al. (2005) tested the BzK selection on a fairly substantial, albeit not uniformly selected, high-redshift spectroscopic sample. They spectroscopically observed a $z \sim 2$ sample in the GOODS-N field selected using the observed U_nGR colors to a limiting AB magnitude of $R=25.5$. These $z \sim 2$ galaxies were selected to be actively star-forming galaxies with the same range in UV properties and extinctions as the LBGs at $z \sim 3$. Adelberger et al. (2004) and Steidel et al. (2004) named sources selected in this way “BX” ($2.0 \leq z \leq 2.6$) and “BM” ($1.5 \leq z \leq 2.0$) galaxies.

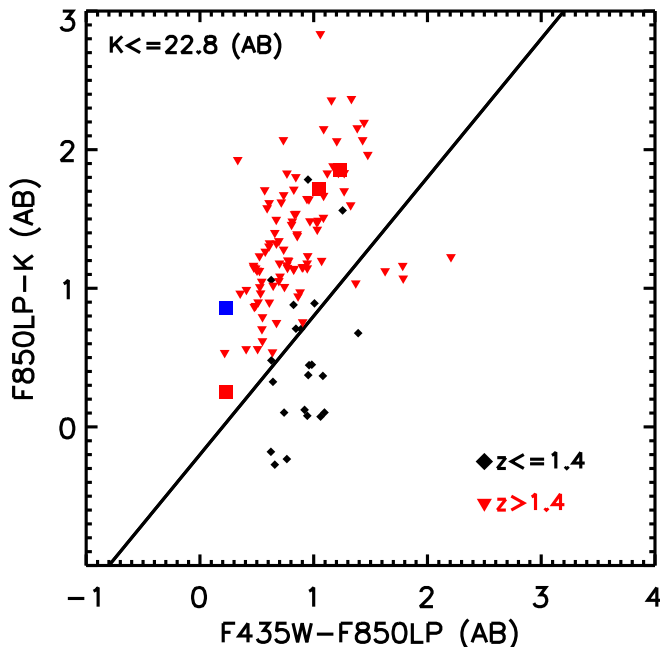


FIG. 9.— $(F850LP - K)_{s,AB}$ vs. $(F435W - F850LP)_{AB}$ for the $15 < K_{s,AB} \leq 22.8$ sources with redshifts from Reddy et al. (2005). The $z \leq 1.4$ galaxies are denoted by black diamonds, and the $z > 1.4$ galaxies are denoted by red upside-down triangles. AGNs are denoted by large squares (blue for $z \leq 1.4$; red for $z > 1.4$). The diagonal line shows the $BzK \geq -0.2$ selection of $z > 1.4$ star-forming galaxies proposed by Daddi et al. (2004).

Reddy et al. (2005) then used a moderately deep K_s image (5σ limit of $K_{s,AB} \sim 23.8$) covering ~ 72.3 arcmin² to put their galaxies on a $K_{s,Vega} \leq 21$ ($K_{s,AB} \leq 22.8$) BzK diagram (see their Fig. 12). For consistency, in Figure 9 we replot their spectroscopic sample on a BzK diagram using our deeper imaging data but restricting to their range $15 < K_{s,AB} \leq 22.8$. We have coded the data points so the $z \leq 1.4$ galaxies (black diamonds) can be differentiated from the $z > 1.4$ galaxies (red upside-down triangles). We denote the AGNs (rest-frame hard or soft X-ray luminosi-

ties $> 10^{42}$ ergs s⁻¹) with large squares (blue for $z \leq 1.4$; red for $z > 1.4$). For this fainter spectroscopic sample the BzK selection still seems to do a reasonably good job of separating the high-redshift galaxies from the low-redshift galaxies, with only a small amount of contamination in either direction (five $z > 1.4$ sources in the low-redshift region; nine $z \leq 1.4$ sources in the high-redshift region, including one AGN). The BzK $z > 1.4$ star-forming galaxy selection completeness is 91% for this sample.

Reddy et al. (2005) claim that the BzK selection completeness decreases slightly at fainter magnitudes, missing about 20% of the $K_{s,AB} > 22.8$ BX/BM galaxies with spectroscopic redshifts $1.4 < z < 2.6$. They point out that a significant fraction of these have colors that place them within $\lesssim 0.2$ mag of the selection window, which is comparable to the photometric uncertainties. Reddy et al. (2005) also found that 11% of their BX/BM candidates with K_s data were undetected to $K_{s,AB} = 24.3$ (3σ). Thus, they conclude that high-redshift sources may be missed from the BzK selection because of photometric scatter or because of insufficiently deep K_s data.

Although we are unable to investigate these issues with a nearly spectroscopically complete sample, we can use just our spectroscopically identified sample to study the selection completeness and selection contamination with increasing magnitude. In Figure 10 we plot two redshift samples separately: (a) $z \leq 1.4$ sources only and (b) $z > 1.4$ sources only. For each we show three magnitude intervals ($15 < K_{s,AB} \leq 21$ - green upside-down triangles; $21 < K_{s,AB} \leq 23$ - red triangles; $23 < K_{s,AB} \leq 24$ - black diamonds) (note that the sources heavily overlap).

With increasing magnitude there is an increasing build-up of sources along the BzK boundary for both redshift intervals. However, in contrast to Reddy et al. (2005)’s conclusion that a substantial fraction of $z > 1.4$ sources are missed by the BzK selection, we find that the selection completeness is extremely good. In total, 254 of the 267 sources with $1.4 < z < 2.8$ (95%) are found with the BzK selection. For the faintest magnitude interval $23 < K_{s,AB} \leq 24$, 69 of the 74 sources with $1.4 < z < 2.8$ (93%) are found. The different conclusion is probably a consequence of the deeper K_s image used here and the corresponding increase in precision in the determination of the BzK parameter.

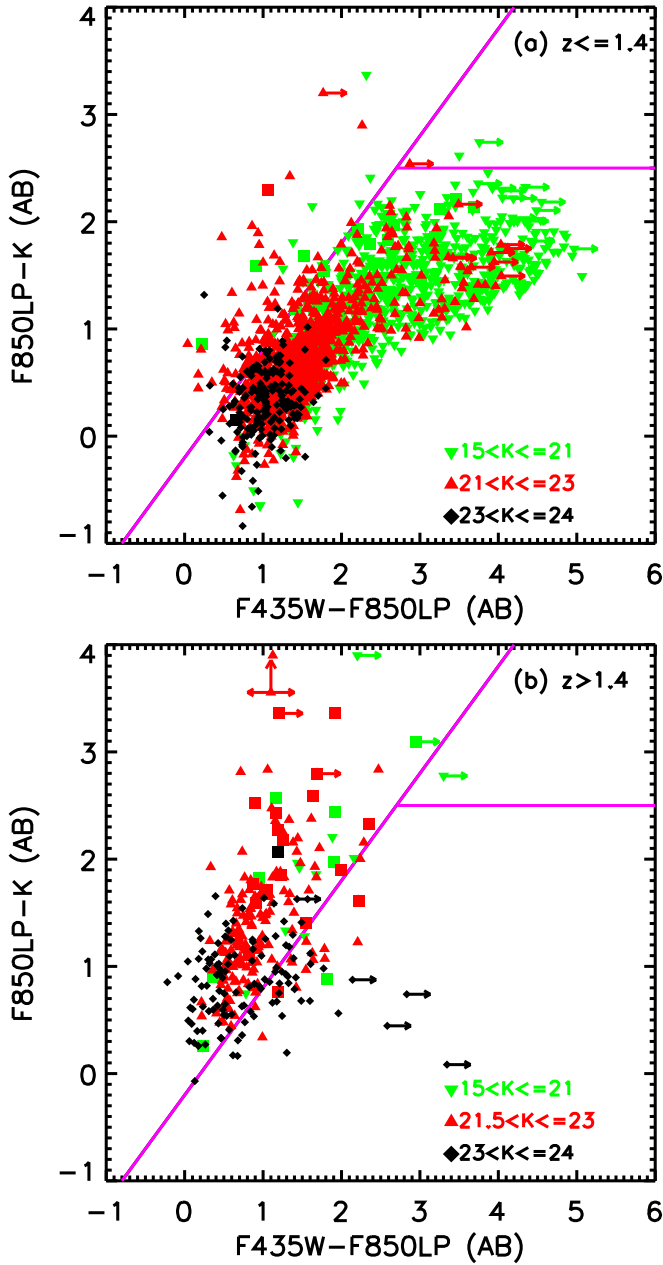


FIG. 10.— $(F850LP - K_s)_{AB}$ vs. $(F435W - F850LP)_{AB}$ for all of the spectroscopically identified $15 < K_{s,AB} \leq 24$ sources with redshifts (a) $z \leq 1.4$ and (b) $z > 1.4$. AGNs are denoted by large squares. Sources with $(F850LP - K_s)_{AB}$ colors redder than 3.9 are shown at that value. The sources are color and symbol coded by magnitude range (see figure legend). The diagonal line shows the $BzK \geq -0.2$ selection of $z > 1.4$ star-forming galaxies. This line combined with the horizontal line shows the $BzK \geq -0.2$, $(F850LP - K_s)_{AB} > 2.5$ selection of passive galaxies at $z > 1.4$. Both were proposed by Daddi et al. (2004).

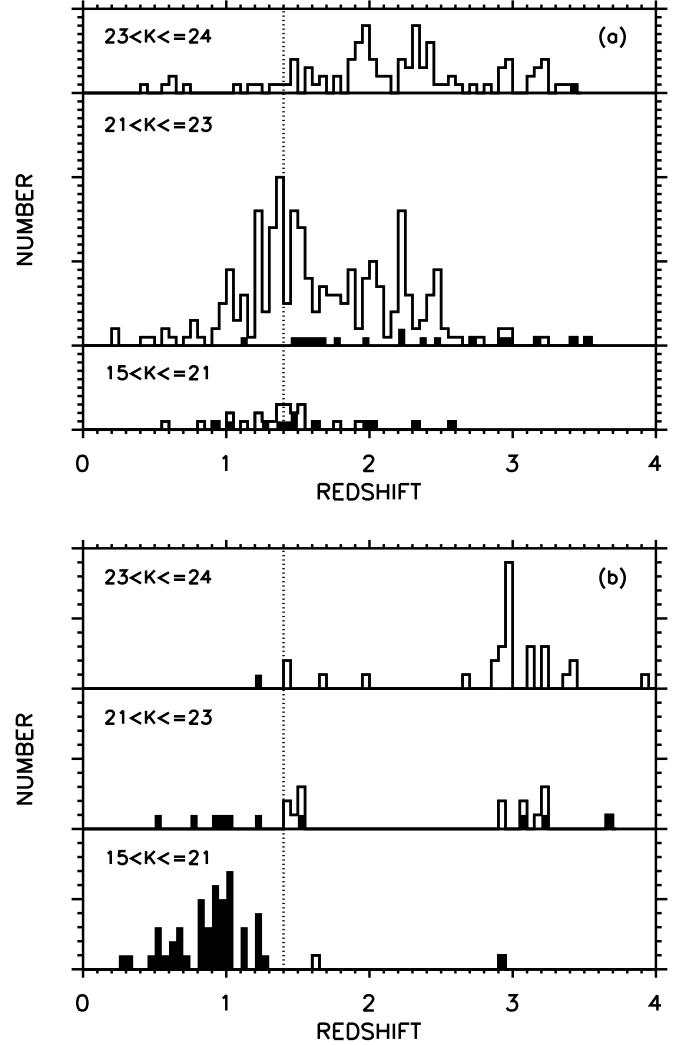


FIG. 11.— Redshift histograms by magnitude interval (see figure labels) for the spectroscopically identified $15 < K_{s,AB} \leq 24$ sources. AGNs are denoted by solid shading. The dotted vertical lines show $z = 1.4$. (a) $BzK \geq -0.2$, the selection of $z > 1.4$ star-forming galaxies proposed by Daddi et al. (2004). (b) $BzK < -0.2$ and $(F850LP - K_s)_{AB} \leq 2.5$ (the latter constraint to exclude passive galaxies at $z > 1.4$). Here only AGNs are shown at $z \leq 1.4$ due to the very large numbers of galaxies at $z \leq 1.4$. Each tick mark on the y-axis represents one source in both panels.

To quantitatively assess what fraction of the spectroscopically identified sources are interlopers on either side of the BzK boundary, in Figure 11 we plot redshift histograms of (a) sources that satisfy the BzK $z > 1.4$ star-forming galaxy criterion and (b) sources that do not. Both figures are divided into the same $K_{s,AB}$ magnitude intervals used in Figure 10. AGNs are denoted by solid shading. Since there are such a large number of galaxies at $z \leq 1.4$, in Figure 11b we only show the AGNs at $z \leq 1.4$. In (a) the sources to the left of the vertical line can be thought of as interlopers in the $z > 1.4$ BzK star-forming region. The contamination is substantial, about 35% in the $21 < K_{s,AB} \leq 23$ interval. In (b) the sources to the right of the vertical line can be thought of as interlopers in the $z \leq 1.4$ region (or as $z > 1.4$ sources missed by the BzK star-forming galaxy selection).

This is consistent with our results from using our highly spectroscopically complete sample at $15 < K_{s,AB} \leq 21$.

A BzK selection picks out nearly all the $z > 1.4$ sources but with a substantial contamination by lower redshift objects. However, it must be remembered that the spectroscopically unidentified sources at these fainter magnitudes may contain substantial biases and that the number of unidentified sources in these fainter magnitude ranges is very large: 1016 unidentified sources (versus 1331 identified) at $21 < K_{s,AB} \leq 23$ and 2083 unidentified sources (versus 311 identified) at $23 < K_{s,AB} \leq 24$.

4.3. H^-

The minimum at $1.6 \mu\text{m}$ in the opacity of the H^- ion present in the atmospheres of cool stars (e.g., John 1988) is seen as a spectral ‘‘bump’’ in the SEDs of all but the youngest (~ 1 Myr) composite stellar populations (see Fig. 1 of Sawicki 2002). Because of its strength and near universality, Simpson & Eisenhardt (1999) and Sawicki (2002) proposed that the $1.6 \mu\text{m}$ bump could be used to obtain photometric redshift measurements for galaxies. However, in using MIR colors as a redshift indicator, one needs to be concerned about the effects of AGN contamination.

Since optically selected luminous AGNs often have red power law SEDs (e.g., Neugebauer et al. 1979; Elvis et al. 1994), several groups have used this characteristic to try to select AGNs in deep surveys using IRAC data (Alonso-Herrero et al. 2006; Donley et al. 2007). Other authors (Lacy et al. 2004; Stern et al. 2005; Hatziminaoglou et al. 2005; Sajina et al. 2005) have proposed that AGNs might be found in a different portion of MIR color-color space than star-forming galaxies. Both of these approaches have been suggested as ways to locate AGNs that may be missed by other techniques.

In Figure 12 we show the $(m_{3.6 \mu\text{m}} - m_{4.5 \mu\text{m}})_{AB}$ versus $(m_{5.8 \mu\text{m}} - m_{8.0 \mu\text{m}})_{AB}$ color-color diagram for all the spectroscopically identified sources in Table 1 with $m_{8.0 \mu\text{m},AB} < 22$ and (a) a rest-frame hard or soft X-ray luminosity $< 10^{42}$ ergs s^{-1} and a radio power $< 10^{31}$ ergs $\text{s}^{-1} \text{Hz}^{-1}$, (b) a rest-frame hard or soft X-ray luminosity $\geq 10^{42}$ ergs s^{-1} , (c) a rest-frame hard or soft X-ray luminosity $< 10^{42}$ ergs s^{-1} and a radio power $\geq 10^{31}$ ergs $\text{s}^{-1} \text{Hz}^{-1}$. We apply the $m_{8.0 \mu\text{m},AB} < 22$ limit because at fainter magnitudes the signal to noise ratio at $8 \mu\text{m}$ is poor and the colors would not be reliable. The $K_{s,AB} < 24.5$ sample should include all of the $m_{8.0 \mu\text{m},AB} < 22$ sources, since sources are fainter at $8 \mu\text{m}$. The spectroscopic completeness of the $m_{8.0 \mu\text{m},AB}$ sample is 94% at $m_{8.0 \mu\text{m},AB} = 21$ and 79% at $m_{8.0 \mu\text{m},AB} = 22$. An ultraluminous infrared galaxy (ULIRG; $L_{\text{FIR}} \geq 4 \times 10^{45}$ ergs s^{-1}) that follows the FIR-radio correlation (Condon 1992) would have a radio power of about 4.8×10^{30} ergs $\text{s}^{-1} \text{Hz}^{-1}$ (Barger et al. 2007). Thus, it is likely that any source with a radio power $\geq 10^{31}$ ergs $\text{s}^{-1} \text{Hz}^{-1}$ is a radio AGN, or at least a very unusual source, which is why we show these sources separately in (c). We will refer to these as high radio power sources hereafter, but their colors are clearly very similar to those of the rest of the sample. In (b) we enclose in black large squares any source with a rest-frame hard or soft X-ray luminosity $\geq 10^{44}$ ergs s^{-1} (X-ray quasar luminosity).

We mark with the green dashed lines the region considered to contain broad-line AGNs by Stern et al. (2005; note that their Fig. 1 shows a few broad-line AGNs and most of

the narrow-line AGNs lying outside this region). We can see from our data that this color-color plot is quite poor at picking out lower luminosity AGNs (see also Barmby et al. 2006; Treister et al. 2006; Donley et al. 2007; Cardamone et al. 2008), while also missing one of the more luminous X-ray AGNs and six of the high radio power sources. It cleanly selects just a few additional AGNs that are not already identified as AGNs based on their X-ray properties, though there are a number of sources on the boundaries (see Figure 12a). Thus, it appears that the AGNs are not significantly contaminating the colors of most of the galaxies, and hence the colors can be used as a redshift measure.

In Figure 12 we divide the galaxies into $z \leq 1.3$ (*black diamonds*) and $z > 1.3$ (*red upside-down triangles*). These two broad redshift categories occupy fairly distinct regions of color-color space, which can be separated by the condition $(m_{3.6 \mu\text{m}} - m_{4.5 \mu\text{m}})_{AB} = 0.24 \times (m_{5.8 \mu\text{m}} - m_{8.0 \mu\text{m}})_{AB}$ (*red solid line*). We hereafter refer to this relation as the H^- selection.

The H^- selection is quite efficient at picking out high-redshift galaxies and AGNs, with 84 of the 94 sources with $m_{8.0 \mu\text{m},AB} < 22$ and $z > 1.3$ satisfying it. This corresponds to a selection completeness of just under 90%. However, there is substantial selection contamination: 53 $z < 1.3$ sources also satisfy the H^- selection, giving a 39% selection contamination. Thus, as with the BzK selection, the H^- selection is a very effective way of finding the high-redshift galaxies, but in order to create a clean sample, spectroscopic follow-up is needed. (Note that Papovich 2008 suggests that an efficient way to reduce the contamination due to $z < 1.0$ interlopers is to apply an apparent magnitude cut.)

If we require the sources to satisfy both the BzK selection and the H^- selection, then we can substantially reduce the selection contamination, but at the expense of reducing the selection completeness to about 80%. However, if we instead require the sources to satisfy one or the other selection, then we can find almost all of the $z > 1.4$ sources (63/64 with $m_{8.0 \mu\text{m},AB} < 22$) at the expense of a high selection contamination (about 55%). This may be the best way to generate a highly complete sample at these redshifts.

Lacy et al. (2004) suggest that interspersed colors, which are a measure of the curvature of the SED, may be more optimal in selecting AGNs. In Figure 13 we show the $(m_{3.6 \mu\text{m}} - m_{5.8 \mu\text{m}})_{AB}$ versus $(m_{4.5 \mu\text{m}} - m_{8.0 \mu\text{m}})_{AB}$ color-color diagram for all the sources in Table 1 with $m_{8.0 \mu\text{m},AB} < 22$ and (a) a rest-frame hard or soft X-ray luminosity $< 10^{42}$ ergs s^{-1} and a radio power $< 10^{31}$ ergs $\text{s}^{-1} \text{Hz}^{-1}$, (b) a rest-frame hard or soft X-ray luminosity $\geq 10^{42}$ ergs s^{-1} , (c) a rest-frame hard or soft X-ray luminosity $< 10^{42}$ ergs s^{-1} and a radio power $\geq 10^{31}$ ergs $\text{s}^{-1} \text{Hz}^{-1}$. In (b) we again enclose in black large squares the sources with a rest-frame hard or soft X-ray luminosity $\geq 10^{44}$ ergs s^{-1} (X-ray quasar luminosity).

We mark with green dashed lines the region considered to contain AGNs by Lacy et al. (2004). This selection is better than the Stern et al. (2005) selection in choosing luminous AGNs, but again it misses some of the lower luminosity sources, as well as three (one is just outside the boundary) of the high radio power sources. However, the galaxy contamination is severe.

In Figure 13 we divide the galaxies into $z \leq 1.6$ (*black diamonds*) and $z > 1.6$ (*red upside-down triangles*). These two broad redshift categories again fall into fairly distinct regions of color-color space, which can be separated by the condition $(m_{3.6 \mu\text{m}} - m_{5.8 \mu\text{m}})_{\text{AB}} = 0.24 \times (m_{4.5 \mu\text{m}} - m_{8.0 \mu\text{m}})_{\text{AB}}$ (*red dashed line*). We hereafter refer to this relation as the IRAC color selection.

The IRAC color selection has a high selection completeness, selecting 47 of the 50 galaxies and AGNs with $m_{8.0 \mu\text{m}} < 22$ and $z > 1.6$. However, once again the contamination by lower redshift sources is substantial (about 40%), and spectroscopic follow-up is necessary to provide a clean sample. As with the H^- selection, requiring the sources to satisfy either the BzK selection or the IRAC color selection can provide an extremely complete selection (49/50 with $m_{8.0 \mu\text{m}, \text{AB}} < 22$ and $z > 1.6$) at the expense of a high selection contamination (about 56%).

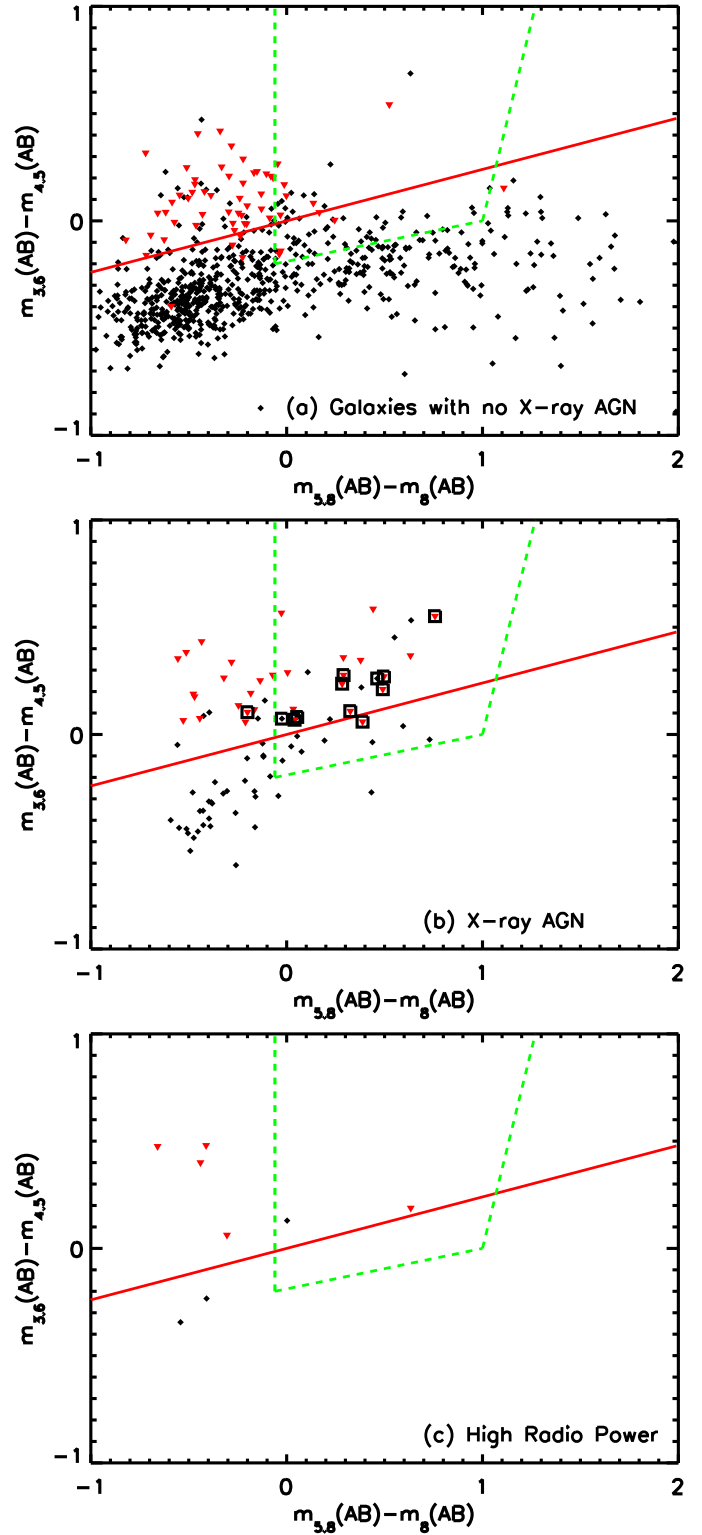


FIG. 12.— $(m_{3.6 \mu\text{m}} - m_{4.5 \mu\text{m}})_{\text{AB}}$ vs. $(m_{5.8 \mu\text{m}} - m_{8.0 \mu\text{m}})_{\text{AB}}$ for all of the spectroscopically identified galaxies with $m_{8.0 \mu\text{m}, \text{AB}} < 22$ and (a) a rest-frame hard or soft X-ray luminosity $< 10^{42}$ ergs s^{-1} and a radio power $< 10^{31}$ ergs s^{-1} Hz^{-1} , (b) a rest-frame hard or soft X-ray luminosity $\geq 10^{42}$ ergs s^{-1} , and (c) a rest-frame hard or soft X-ray luminosity $< 10^{42}$ ergs s^{-1} and a radio power $\geq 10^{31}$ ergs s^{-1} Hz^{-1} . Sources with $z \leq 1.3$ ($z > 1.3$) are shown as black diamonds (red upside-down triangles). AGNs with quasar X-ray luminosities are enclosed in black large squares. The diagonal red solid line shows the condition $(m_{3.6 \mu\text{m}} - m_{4.5 \mu\text{m}})_{\text{AB}} = 0.24 \times (m_{5.8 \mu\text{m}} - m_{8.0 \mu\text{m}})_{\text{AB}}$, which roughly divides the sources in both panels at $z = 1.3$. The green dashed lines enclose the region where Stern et al. (2005) suggested that these MIR colors select out most broad-line AGNs.

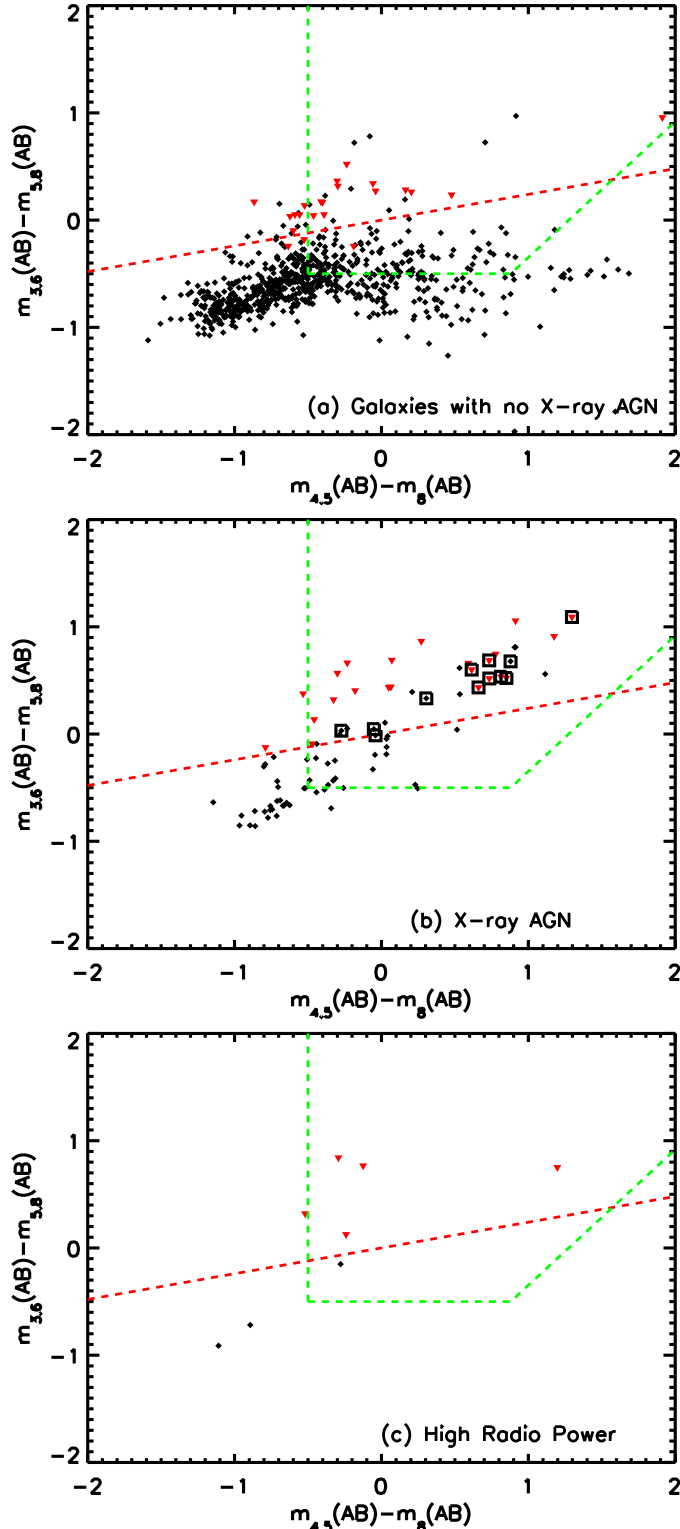


FIG. 13.— $(m_{3.6 \mu\text{m}} - m_{3.8 \mu\text{m}})_{\text{AB}}$ vs. $(m_{4.5 \mu\text{m}} - m_{8.0 \mu\text{m}})_{\text{AB}}$ for all of the spectroscopically identified galaxies with $m_{8.0 \mu\text{m}, \text{AB}} < 22$ and (a) a rest-frame hard or soft X-ray luminosity $< 10^{42}$ ergs s^{-1} and a radio power $< 10^{31}$ ergs s^{-1} Hz^{-1} , (b) a rest-frame hard or soft X-ray luminosity $\geq 10^{42}$ ergs s^{-1} , and (c) a rest-frame hard or soft X-ray luminosity $< 10^{42}$ ergs s^{-1} and a radio power $\geq 10^{31}$ ergs s^{-1} Hz^{-1} . Sources with $z \leq 1.6$ ($z > 1.6$) are shown as black diamonds (red upside-down triangles). AGNs with quasar luminosities are enclosed in black large squares. The diagonal red dashed line shows the condition $(m_{3.6 \mu\text{m}} - m_{3.8 \mu\text{m}})_{\text{AB}} = 0.24 \times (m_{4.5 \mu\text{m}} - m_{8.0 \mu\text{m}})_{\text{AB}}$, which roughly divides the sources in both panels at $z = 1.6$. The green dashed lines enclose the region where Lacy et al. (2004) suggested that these MIR colors select out AGNs.

5. INTERGALACTIC MEDIUM TOMOGRAPHY

One interesting application of this data set is to investigate the feasibility of one of the major science projects proposed for a 30 m telescope: tomography of the IGM. The goal of the tomography project is to observe sufficient numbers of background sources (galaxies and AGNs) to have enough lines of sight to probe the distribution of the intervening gas. The Thirty Meter Telescope (TMT) Science Advisory Committee (2007) estimated that $R \sim 24.5$ is approximately the apparent magnitude at which TMT/WFOS can obtain a spectrum at a spectral resolution of 6000 with a signal-to-noise ratio (S/N) of about 30 (see their Figure 5-12 for a simulated spectrum of an $R = 24$ galaxy observed with WFOS). The high-resolution ACS images of the present data set allow us to model this in more detail by correctly including the slit losses. Here we do this by measuring the S/N, which can be obtained with an optimal positioning of each galaxy in the slit and for a given natural seeing.

For the telescope and spectrograph properties, we follow the TMT Observatory Requirements Document (2007). We take the telescope's collecting area to be 655 m^2 . (The proposed Giant Magellan Telescope has an area of 368 m^2 , and the exposure times would be nearly doubled.) We assume a $0.75''$ wide slit and a spectral resolution of 6000 for the instrumental parameters. We take a typical sky to collection efficiency of 25%, though the peak efficiency could be slightly higher than this. We assume a 10 hr integration.

We calculate the S/N at the central wavelength (6060 \AA) of the F606W filter. Longer wavelengths are in the complex OH night sky spectrum, and hence the calculation of the S/N becomes extremely wavelength dependent. However, at 6060 \AA we can assume a smooth continuum sky brightness. The choice of sky brightness is not straightforward, since it is somewhat variable and site dependent. We adopt a continuum AB surface brightness of $21.4 \text{ mags arcsec}^{-2}$ at this wavelength, which is based on the mean zenith V ($21.7 \text{ mags arcsec}^{-2}$) and R ($21.1 \text{ mags arcsec}^{-2}$) AB surface brightnesses at Cerro Paranal (Patat 2003). (The V -band sky background at Mauna Kea is similar; Krisciunas 1997.) We have also corrected for the strong emission line contributions, and we have assumed that the galaxy is being observed at an average airmass of 1.3. The choice of the sky background is probably the largest uncertainty in our calculation.

We use the point spread function determined from stars in the MOIRCS K_s image with an appropriate scaling to smooth the ACS images to the desired ground-based seeing. For our reference calculation we adopt a high-quality seeing of $0.65''$, assuming that these observations would be prioritized to optimal times. We show a typical $z = 2.05$ galaxy with respect to the $0.75''$ wide slit in Figure 14 at (a) the original ACS resolution and (b) the ground-based seeing. We place each galaxy in an optimal position in the slit and compute the S/N which would be obtained in an optimal spectral extraction of the light distribution along the slit. Because the noise is sky-dominated, the fainter portions of the light profile do not contribute much to the S/N. In Figure 15 we show the expected S/N per resolu-

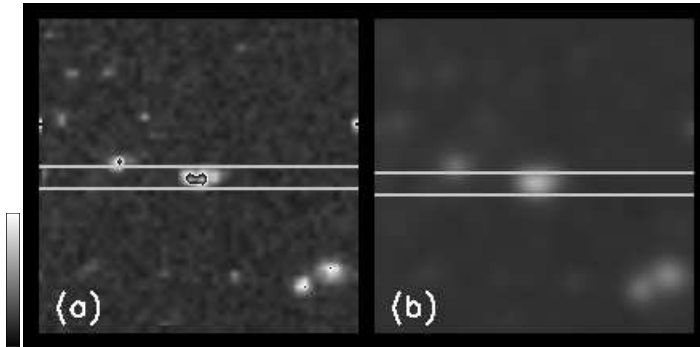


FIG. 14.— A $F606W_{AB} = 24$ galaxy at $z = 2.05$ (a) before and (b) after smoothing to $0.65''$ ground-based seeing. The white lines show the position of the $0.75''$ wide slit.

tion element for all the galaxies (*black squares*) and AGNs (*red large squares*) with $F606W_{AB} < 25$ and known redshifts in the (a) $z = 2 - 3$ and (b) $z = 3 - 4$ ranges versus $F606W$ magnitude.

We test our S/N calculation using the spectrum of the brightest AGN in the $z = 2 - 3$ range in the ACS GOODS-N field, the source with $F606W_{AB} = 20.5$ in Figure 15a. The redshift of this source is $z = 2.6$. We use a 1.5 hr spectrum obtained with the Echellette Spectrograph and Imager (ESI; Epps & Miller 1998; Sheinis et al. 2000) on the Keck II telescope from A. Songaila (2008, in preparation). The observation was made with a $0.75''$ wide slit under $0.9''$ seeing with some windshake. The spectral resolution is 5400. We show a segment of the spectrum around 6000 \AA in Figure 16. The measured S/N is 40 in a resolution element, while our S/N calculation gives a value of 45 for a 1.5 hr exposure on a 10 m telescope at this seeing. The slight degradation may be a consequence of windshake effects on the guiding or of imperfections in the extraction of the spectrum, but overall the agreement is excellent.

The choice of S/N for the tomographic project is complex. If we simply want to identify kinematic structures, then we can tolerate lower S/N spectra, but if we wish to measure column densities and abundances, then we need high S/N spectra. In general the strong lines which can be measured in a low-resolution spectrum with low S/N are saturated, and it is not possible to derive accurate column densities using them (e.g., Jenkins 1986; Prochaska 2007). Prochaska (2007) shows that in order to measure weak lines where useful information on the column densities can be derived, we need to detect rest-frame equivalent widths of 100 m\AA or less. For a 5σ measurement of a 100 m\AA absorption-line system at $z = 1$, this translates to a S/N of 25 per resolution element at a spectral resolution of 6000, which seems a reasonable figure of merit. However, the surface density of sources is extremely sensitive to the limiting magnitude, since we are on the exponential tail of the galaxy distribution. In Figure 15 we show two S/N values that bracket the above figure of merit: S/N of 20 and S/N of 30 per resolution element (*blue horizontal lines*). These intersect with the galaxy track at magnitudes of $F606W_{AB} = 24.2$ and 23.7 (*vertical dashed lines*), respectively, for the $z = 2 - 3$ and $z = 3 - 4$ redshift intervals, resulting in substantially different surface densities.

To quantify this, in Figure 17 we show the cumulative surface densities of sources (galaxies and AGNs) in the ACS GOODS-N field versus $F606W_{AB}$ magnitude for the redshift intervals (a) $z = 2 - 3$ and (b) $z = 3 - 4$. We de-

note all sources together by black diamonds with 1σ uncertainties (*black solid curves*) and AGNs alone by red open squares with (in Fig. 17a) 1σ uncertainties (*red dashed curves*). We obtain maximum surface densities by putting all of the spectroscopically unidentified sources into each redshift interval (*blue curves*).

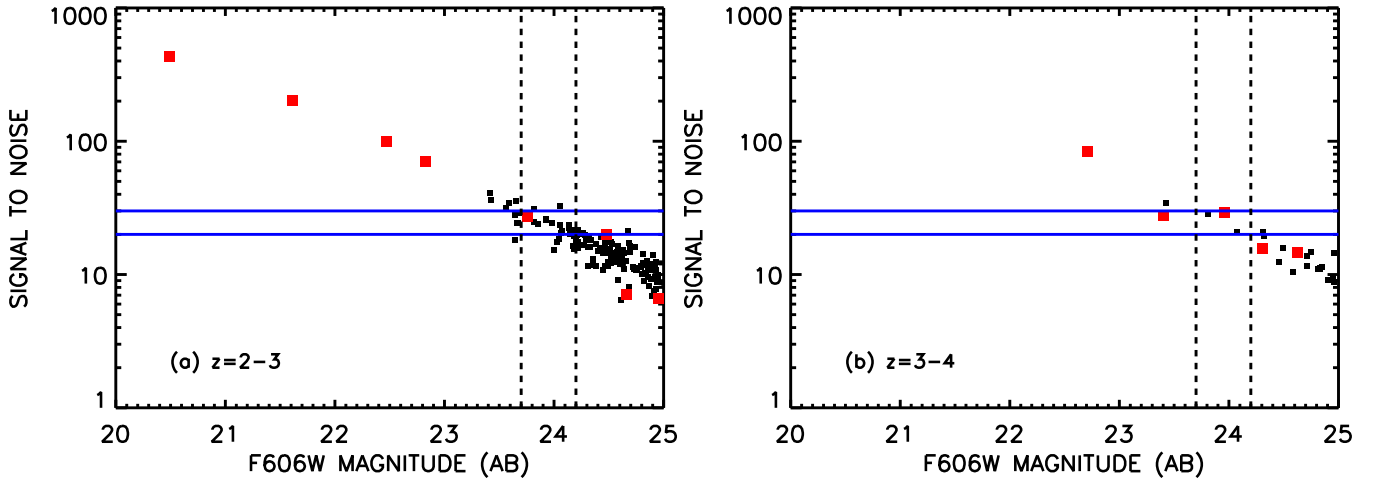


FIG. 15.— Expected S/N per resolution element vs. F606W magnitude for a 30 m telescope and an exposure time of 10 hr for the sources (galaxies and AGNs) in the redshift intervals (a) $z = 2 - 3$ and (b) $z = 3 - 4$ in the ACS GOODS-N field. The adopted seeing is $0.65''$, the spectral resolution is 6000, and the slit width is $0.75''$. AGNs are denoted by red large squares. The blue horizontal lines mark S/N per resolution element values of 20 and 30, and the black vertical dashed lines show the F606W AB magnitudes (24.2 and 23.7, respectively) at which these S/N values are reached for a typical galaxy.

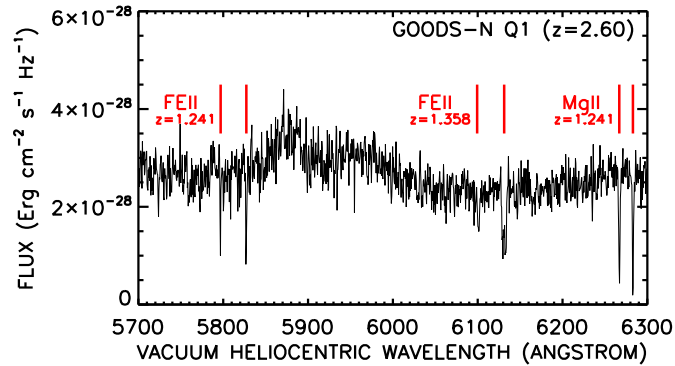


FIG. 16.— Spectrum of the brightest AGN in the $z = 2 - 3$ range in the ACS GOODS-N field (Songaila 2008, in preparation). The spectrum is a 1.5 hr exposure with a spectral resolution of 5400 obtained with a $0.75''$ wide slit under $0.9''$ seeing using ESI on Keck II. The spectrum is shown with pixels spaced to Nyquist sample the resolution, and the S/N is 40 per resolution element. Fe and Mg lines from two absorption systems at $z = 1.241$ and $z = 1.358$ are marked with the red lines.

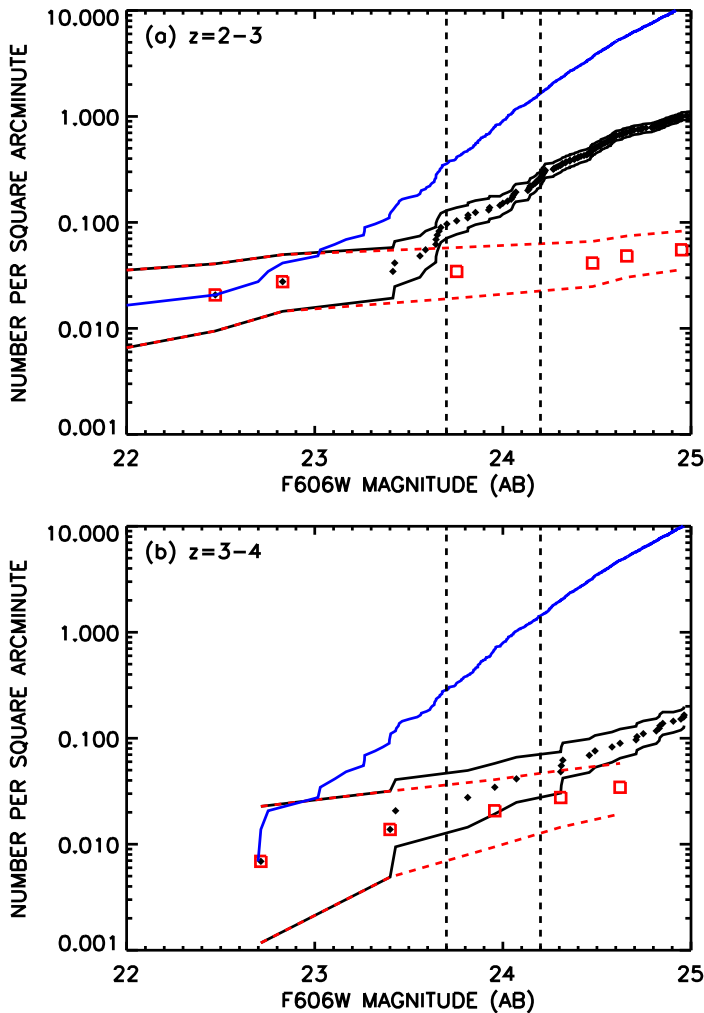


FIG. 17.— Cumulative surface densities of sources (galaxies and AGNs) in the ACS GOODS-N field vs. $F606W_{AB}$ magnitude for the redshift intervals (a) $z = 2 - 3$ and (b) $z = 3 - 4$ (black diamonds with black solid curves for the 1σ uncertainties). AGNs alone are shown with red open squares. The red dashed curves in (a) show the 1σ uncertainties for the AGNs. The maximum surface densities for the two redshift intervals are obtained by placing all of the spectroscopically unidentified sources into each redshift interval (blue curves). The black vertical dashed lines show the $F606W_{AB}$ magnitudes (24.2 and 23.7, respectively, for S/N per resolution element values of 20 and 30).

We can see from Figure 17a that at magnitudes significantly brighter than $F606W_{AB} = 23.7$ the cumulative surface densities are still dominated by AGNs, and it is only near $F606W_{AB} = 24$ that galaxies begin to dominate. After allowing for the maximum possible correction in each redshift interval, the upper bound on the surface densities is $\lesssim 1.5 \text{ arcmin}^{-2}$ at $F606W_{AB} = 24.2$ ($S/N = 20$) in both the $z = 2 - 3$ and $z = 3 - 4$ ranges. This is an extreme upper limit, since the unidentified galaxies will not all lie in an individual redshift range and many may lie below $z = 2$. At $F606W_{AB} = 23.7$ ($S/N = 30$) the upper bound on the surface densities in both the $z = 2 - 3$ and $z = 3 - 4$ ranges is $\lesssim 0.4 \text{ arcmin}^{-2}$. Again this is an extreme upper limit, and the true value may be closer to the measured source value of 0.1 arcmin^{-2} in the $z = 2 - 3$ range. For a 10 m telescope the limiting magnitudes are 1.2 mag brighter, which means the surface densities that can be observed with a 30 m telescope are a factor of 5 to 20 higher than

those which can be achieved with a 10 m telescope (e.g., 0.02 arcmin^{-2} at $F606W_{AB} = 22.5$ for $z = 2 - 3$ and $S/N = 30$).

We conclude that with a 30 m telescope it will be possible to study examples of near neighbors and to map regions at arcminute scales. However, tomography at the sub-arcminute level is probably still beyond the reach of even an ideal 30 m telescope.

6. SUMMARY

In this paper we presented deep K_s -band imaging and the most spectroscopically complete redshift sample obtained to date of the 145 arcmin^2 *HST* ACS GOODS-N region. We provided the data in a variety of tables as a function of magnitude from the NUV to the MIR. The redshift identifications are greater than 90% complete to magnitudes of $F435W_{AB} = 24.5$, $F850LP_{AB} = 23.3$, and $K_{s,AB} = 21.5$ and to $24 \mu\text{m}$ fluxes of $250 \mu\text{Jy}$.

We used the data to analyze various color selection techniques that have been proposed to find high-redshift galaxies. The LBG technique still appears to be the most robust method for providing a high selection completeness with low contamination. We do not confirm the presence of additional luminous galaxies not picked out by the LBG selection, as proposed by Le Fèvre et al. (2005). BzK , H^- , and IRAC color techniques can be highly efficient at selecting high-redshift ($z > 1.4$, $z > 1.3$, and $z > 1.6$, respectively) galaxies and AGNs but at the expense of a fairly high degree of contamination by lower redshift galaxies. Samples selected using these techniques therefore need to be spectroscopically followed up in order to obtain clean high-redshift samples.

Finally, we have used the ACS images to make detailed calculations of the S/N which can be obtained with spectral resolution 6000 seeing-limited spectra on a 30 m telescope. We find that spectra with $S/N \geq 30$ per resolution element in 10 hr integrations can only be obtained for galaxies brighter than $F606W_{AB} = 23.7$. We have also computed the observed cumulative surface densities of galaxies and AGNs as a function of magnitude in the $z = 2 - 3$ and $z = 3 - 4$ ranges, as well as the maximum surface densities which could lie in these intervals when unidentified sources are included. These surface densities suggest that moderate spectral resolution (6000) observations with $S/N \geq 30$ on a 30 m telescope will still primarily be of the AGN population and that the samples will be sparse with average separations greater than 1 arcmin at $z = 2 - 4$.

We thank the anonymous referee for a helpful report. We gratefully acknowledge support from NSF grants AST 0239425 and AST 0708793 (A. J. B.) and AST 0407374 and AST 0709356 (L. L. C.), the University of Wisconsin Research Committee with funds granted by the Wisconsin Alumni Research Foundation, and the David and Lucile Packard Foundation (A. J. B.). We would like to thank Greg Wirth, Jim Lyke, Marc Kassis, and Grant Hill for their unstinting help with DEIMOS through the course of this project. This research used the facilities of the Canadian Astronomy Data Centre operated by the National Research Council of Canada with the support of the Canadian Space Agency. Based in part on data collected at Subaru Telescope and obtained from the SMOKA, which is

operated by the Astronomy Data Center, National Astronomical Observatory of Japan. Some of the data presented in this paper were obtained from the Multimission Archive at the Space Telescope Science Institute (MAST). STScI is operated by the Association of Universities for Research

in Astronomy, Inc., under NASA contract NAS5-26555. Support for MAST for non-HST data is provided by the NASA Office of Space Science via grant NAG5-7584 and by other grants and contracts.

REFERENCES

- Abraham, R. G., et al. 2004, *AJ*, 127, 2455
 Adelberger, K. L., Steidel, C. C., Shapley, A. E., Hunt, M. P., Erb, D. K., Reddy, N. A., & Pettini, M. 2004, *ApJ*, 607, 226
 Alexander, D. M., et al. 2003, *AJ*, 126, 539
 Alonso-Herrero, A., et al. 2006, *ApJ*, 640, 167
 Barger, A. J., et al. 2003, *AJ*, 126, 632
 Barger, A. J., Cowie, L. L., & Wang, W.-H. 2007, *ApJ*, 654, 764
 Barmby, P., et al. 2006, *ApJ*, 642, 126
 Bertin, E., & Arnouts, S. 1996, *A&AS*, 117, 393
 Bruzual, G., & Charlot, S. 2003, *MNRAS*, 344, 1000
 Capak, P., et al. 2004, *AJ*, 127, 180
 Cardamone, C. N., et al. 2008, *ApJ*, 680, 130
 Chapman, S. C., Blain, A. W., Smail, I., & Ivison, R. J. 2005, *ApJ*, 622, 772
 Chapman, S. C., Smail, I., Blain, A. W., & Ivison, R. J. 2004, *ApJ*, 614, 671
 Cimatti, A., et al. 2002, *A&A*, 392, 395
 Cohen, J. G. 2001, *AJ*, 121, 2895
 Cohen, J. G., et al. 2000, *ApJ*, 538, 29
 Condon, J. J. 1992, *ARA&A*, 30, 575
 Cowie, L. L., & Barger, A. J. 2008, *ApJ*, 686, 72
 Cowie, L. L., Barger, A. J., Hu, E. M., Capak, P., & Songaila, A. 2004, *AJ*, 127, 3137
 Cowie, L. L., Barger, A. J., & Trouille, L. 2008, *ApJ*, in press (arXiv:0811.1042)
 Cowie, L. L., Lilly, S. J., Gardner, J., & McLean, I. S. 1988, *ApJ*, 332, L29
 Cowie, L. L., Songaila, A., Hu, E. M., & Cohen, J. G. 1996, *AJ*, 112, 839
 Daddi, E., Cimatti, A., Renzini, A., Fontana, A., Mignoli, M., Pozzetti, L., Tozzi, P., & Zamorani, G. 2004, *ApJ*, 617, 746
 Daddi, E., Dannerbauer, H., Elbaz, D., Dickinson, M., Morrison, G., Stern, D., & Ravindranath, S. 2008, *ApJ*, 673, L21
 Dawson, S., Stern, D., Bunker, A., Spinrad, H., & Dey, A. 2001, *AJ*, 122, 598
 Donley, J. L., Rieke, G. H., Pérez-González, P. G., Rigby, J. R., & Alonso-Herrero, A. 2007, *ApJ*, 660, 167
 Elvis, M., et al. 1994, *ApJS*, 95, 1
 Epps, H., & Miller, J. S. 1998, *Proc. SPIE*, 3355, 48
 Faber, S. M., et al. 2003, *Proc. SPIE*, 4841, 1657
 Fazio, G., et al. 2004, *ApJS*, 154, 10
 Franx, M., et al. 2003, *ApJ*, 587, L79
 Giavalisco, M., et al. 2004, *ApJ*, 600, L93
 Grazian, A., et al. 2007, *A&A*, 465, 393
 Hatziminaoglou, E., et al. 2005, *AJ*, 129, 1198
 Hawarden, T. G., Leggett, S. K., Letawsky, M. B., Ballantyne, D. R., & Casali, M. M. 2001, *MNRAS*, 325, 563
 Jenkins, E. B. 1986, *ApJ*, 304, 739
 John, T. L. 1988, *A&A*, 193, 189
 Kajisawa, M., et al. 2006, *PASJ*, 58, 951
 Kong, X., et al. 2006, *ApJ*, 638, 72
 Krisciunas, K. 1997, *PASP*, 109, 1181
 Lacy, M., et al. 2004, *ApJS*, 154, 166
 Lane, K. P., et al. 2007, *MNRAS*, 379, L25
 Le Fèvre, O., et al. 2005, *Nature*, 437, 519
 Lilly, S. J., Cowie, L. L., & Gardner, J. 2001, *ApJ*, 389, 79
 Lowenthal, J. D., et al. 1997, *ApJ*, 481, 673
 Martin, D. C., et al. 2005, *ApJ*, 619, L1
 Moran, E. C., Lehnert, M. D., & Helfand, D. J. 1999, *ApJ*, 526, 649
 Neugebauer, G., Oke, J. B., Becklin, E. E., & Matthews, K. 1979, *ApJ*, 230, 79
 Oke, J. B., et al. 1995, *PASP*, 107, 375
 Paltani, S., et al. 2007, *A&A*, 463, 873
 Papovich, C. 2008, *ApJ*, 676, 206
 Patat, F. 2003, *A&A*, 400, 1183
 Phillips, A. C., Guzman, R., Gallego, J., Koo, D. C., Lowenthal, J. D., Vogt, N. P., Faber, S. M., & Illingworth, G. D. 1997, *ApJ*, 489, 543
 Pope, A., et al. 2008, *ApJ*, 675, 1171
 Popesso, P., et al. 2008, *A&A*, in press (arXiv:0802.2930)
 Prochaska, J. X. 2007, *ApJ*, 650, 272
 Quadri, R., et al. 2007, *ApJ*, 654, 138
 Reddy, N. A., Erb, D. K., Steidel, C. C., Shapley, A. E., Adelberger, K. L., & Pettini, M. 2005, *ApJ*, 633, 748
 Reddy, N. A., Steidel, C. C., Erb, D. K., Shapley, A. E., & Pettini, M. 2006, *ApJ*, 653, 1004
 Richards, E. A. 2000, *ApJ*, 533, 611
 Rieke, G., et al. 2004, *ApJS*, 154, 25
 Sajina, A., Lacy, M., & Scott, D. 2005, *ApJ*, 621, 256
 Sawicki, M. 2002, *AJ*, 124, 3050
 Sheinis, A. I., Miller, J. S., Bolte, M., & Sutun, B. M. 2000, *Proc. SPIE*, 4008, 522
 Simpson, C., & Eisenhardt, P. 1999, *PASP*, 111, 691
 Songaila, A., Cowie, L. L., & Lilly, S. J. 2000, *ApJ*, 348, 371
 Steidel, C. C., Adelberger, K. L., Giavalisco, M., Dickinson, M., & Pettini, M. 1999, *ApJ*, 519, 1
 Steidel, C. C., Adelberger, K. L., Shapley, A. E., Pettini, M., Dickinson, M., & Giavalisco, M. 2003, *ApJ*, 692, 728
 Steidel, C. C., Giavalisco, M., Pettini, M., Dickinson, M., & Adelberger, K. L. 1996, *ApJ*, 462, L17
 Steidel, C. C., & Hamilton, D. 1993, *AJ*, 105, 2017
 Steidel, C. C., Pettini, M., & Hamilton, D. 1995, *AJ*, 110, 2519
 Steidel, C. C., Shapley, A. E., Pettini, M., Adelberger, K. L., Erb, D. K., Reddy, N. A., & Hunt, M. P. 2004, *ApJ*, 604, 534
 Stern, D., et al. 2005, *ApJ*, 631, 163
 Swinbank, A. M., Smail, I., Chapman, S. C., Blain, A. W., Ivison, R. J., & Keel, W. C. 2004, *ApJ*, 617, 64
 TMT Observatory Requirements Document: 2007, ed. G. Angeli, & S. Roberts, TMT Document Number: TMT.SEN.DRD.05.001.CCR18
 TMT Science Advisory Committee 2007, in Thirty Meter Telescope Detailed Science Case: 2007, ed. D. Silva, P. Hickson, C. C. Steidel, & M. Bolte, TMT Document Number: TMT.PSC.TEC.07.003.REL01
 Tokunaga, A. T., Simons, D. A., & Vacca, W. D. 2002, *PASP*, 114, 180
 Treister, E., et al. 2006, *ApJ*, 640, 603
 Treu, T., Ellis, R. S., Liao, T. X., van Dokkum, P. G. 2005, *ApJ*, 622, L5
 Trouille, L. T., Barger, A. J., Cowie, L. L., Yang, Y., & Mushotzky, R. F. 2008, *ApJS*, 179, 1
 van Dokkum, P. G., et al. 2003, *ApJ*, 587, L83
 Wirth, G. D., et al. 2004, *AJ*, 127, 3121
 Zezas, A. L., Georgantopoulos, I., & Ward, M. J. 1998, *MNRAS*, 301, 915

TABLE 5
SPECTROSCOPICALLY IDENTIFIED FRACTION FOR THE OPTICAL AND NIR SAMPLES

| Band | 98% | 95% | 90% | 80% |
|--------|------|------|------|------|
| F435W | 23.9 | 24.2 | 24.5 | 24.9 |
| F606W | 23.6 | 23.9 | 24.2 | 24.5 |
| F775W | 23.1 | 23.4 | 23.6 | 24.0 |
| F850LP | 22.6 | 22.9 | 23.3 | 23.7 |
| K_s | 20.7 | 21.0 | 21.5 | 22.2 |

TABLE 6
SOURCE OF SPECTROSCOPIC REDSHIFTS

| Source (1) | Number (2) | Unique ^a (3) | Cumulative (4) | Reference (5) |
|---------------|---------------|----------------------------|-------------------|-----------------------------------------------------|
| 1 | 1506 | 842 | 1506 | This work; see also Cowie et al. (2004) |
| 2 | 1389 | 557 | 2551 | TKRS; Wirth et al. (2004) |
| 3 | 394 | 19 | 2581 | Our LRIS spectra |
| 4 | 343 | 224 | 2853 | Reddy et al. (2006) |
| 5 | 613 | 13 | 2879 | Cohen et al. (2000, 2001) |
| 6 | 114 | 1 | 2880 | Lowenthal et al. (1997); Phillips et al. (1997) |
| 7 | 243 | 2 | 2882 | Treu et al. (2005) |
| 8 | 14 | 8 | 2890 | Chapman et al. (2004, 2005); Swinbank et al. (2004) |
| 9 | 50 | 3 | 2893 | Steidel et al. (2003) |
| 10 | 44 | 5 | 2898 | Dawson et al. (2001) |
| 11 | 4 | 4 | 2902 | Pope et al. (2008) |
| 12 | 0 | 0 | 2902 | Barger et al. (2003) ^b |
| 13 | 2 | 0 | 2902 | Daddi et al. (2008) |
| 14 | 8 | 1 | 2903 | MOIRCS spectra |

^aThe number of sources for which only that catalog has obtained redshift identifications.

^bWe have not distinguished the observations made in the Barger et al. (2003) paper (literature source 12) from our DEIMOS and LRIS observations of the ACS GOODS-N area (literature sources 1 and 3), which is why zeros appear in the number and unique columns for Barger et al. (2003). However, we retain Barger et al. (2003) as a literature source in this table because it includes some ESI identifications which appear in the 24 μ m catalog outside the ACS GOODS-N area.